

A discrete ‘early-responder’ stromal-cell subtype orchestrates immunocyte recruitment to injured tissue

Received: 15 July 2022

Accepted: 5 October 2023

Published online: 6 November 2023

 Check for updates

Omar K. Yaghi^{1,2,3}, Bola S. Hanna^{1,2,3}, P. Kent Langston^{1,2}, Daniel A. Michelson^{1,2}, Teshika Jayewickreme^{1,2}, Miguel Marin-Rodero^{1,2}, Christophe Benoist^{1,2} & Diane Mathis^{1,2} ✉

Following acute injury, stromal cells promote tissue regeneration by a diversity of mechanisms. Time-resolved single-cell RNA sequencing of muscle mesenchymal stromal cells (MmSCs) responding to acute injury identified an ‘early-responder’ subtype that spiked on day 1 and expressed a notable array of transcripts encoding immunomodulators. IL-1 β , TNF- α and oncostatin M each strongly and rapidly induced MmSCs transcribing this immunomodulatory program. Macrophages amplified the program but were not strictly required for its induction. Transfer of the inflammatory MmSC subtype, tagged with a unique surface marker, into healthy hindlimb muscle induced inflammation primarily driven by neutrophils and macrophages. Among the abundant inflammatory transcripts produced by this subtype, *Cxcl5* was stroma-specific and highly upregulated with injury. Depletion of this chemokine early after injury revealed a substantial impact on recruitment of neutrophils, a prolongation of inflammation to later times and an effect on tissue regeneration. Mesenchymal stromal cell subtypes expressing a comparable inflammatory program were found in a mouse model of muscular dystrophy and in several other tissues and pathologies in both mice and humans. These ‘early-responder’ mesenchymal stromal cells, already in place, permit rapid and coordinated mobilization and amplification of critical cell collaborators in response to injury.

Upon acute skeletal muscle injury, local muscle stem cells (MuSCs) become activated, proliferate, differentiate into myotubes and eventually fuse to damaged myofibers^{1–4}. Loss of this MuSC response results in complete abrogation of tissue repair^{5–7}. The immune system similarly undergoes a dynamic and orchestrated reaction to acute muscle injury, involving rapid infiltration of neutrophils (NFs), followed by accumulation of inflammatory and subsequently reparative macrophages (MFs)^{8–17}. Later, adaptive immunocytes, such as Foxp3⁺ CD4⁺ conventional T (T_{conv}) cells and Foxp3⁺ CD4⁺ regulatory T (T_{reg}) cells, accrue at

the injury site^{15,16,18–20}. If key elements of this sequence are disrupted, muscle regeneration is compromised^{9,13,14,17–20}.

Muscle mesenchymal stromal cells (MmSCs), which encompass fibro-adipogenic progenitors, are another cell type that are important for effective muscle regeneration^{21,22}. Depending on the stimulus, these cells can differentiate into fibroblasts, adipocytes, chondrocytes or osteocytes^{23–27}. In various chronic muscle diseases, they are associated with pathological fibrosis and fat deposition^{23–25,28–34}. Nonetheless, after acute muscle injury, MmSCs promote proliferation, commitment

¹Department of Immunology, Harvard Medical School, Boston, MA, USA. ²Evergrande Center for Immunologic Diseases, Harvard Medical School and Brigham and Women’s Hospital, Boston, MA, USA. ³These authors contributed equally: Omar K. Yaghi, Bola S. Hanna. ✉e-mail: dm@hms.harvard.edu

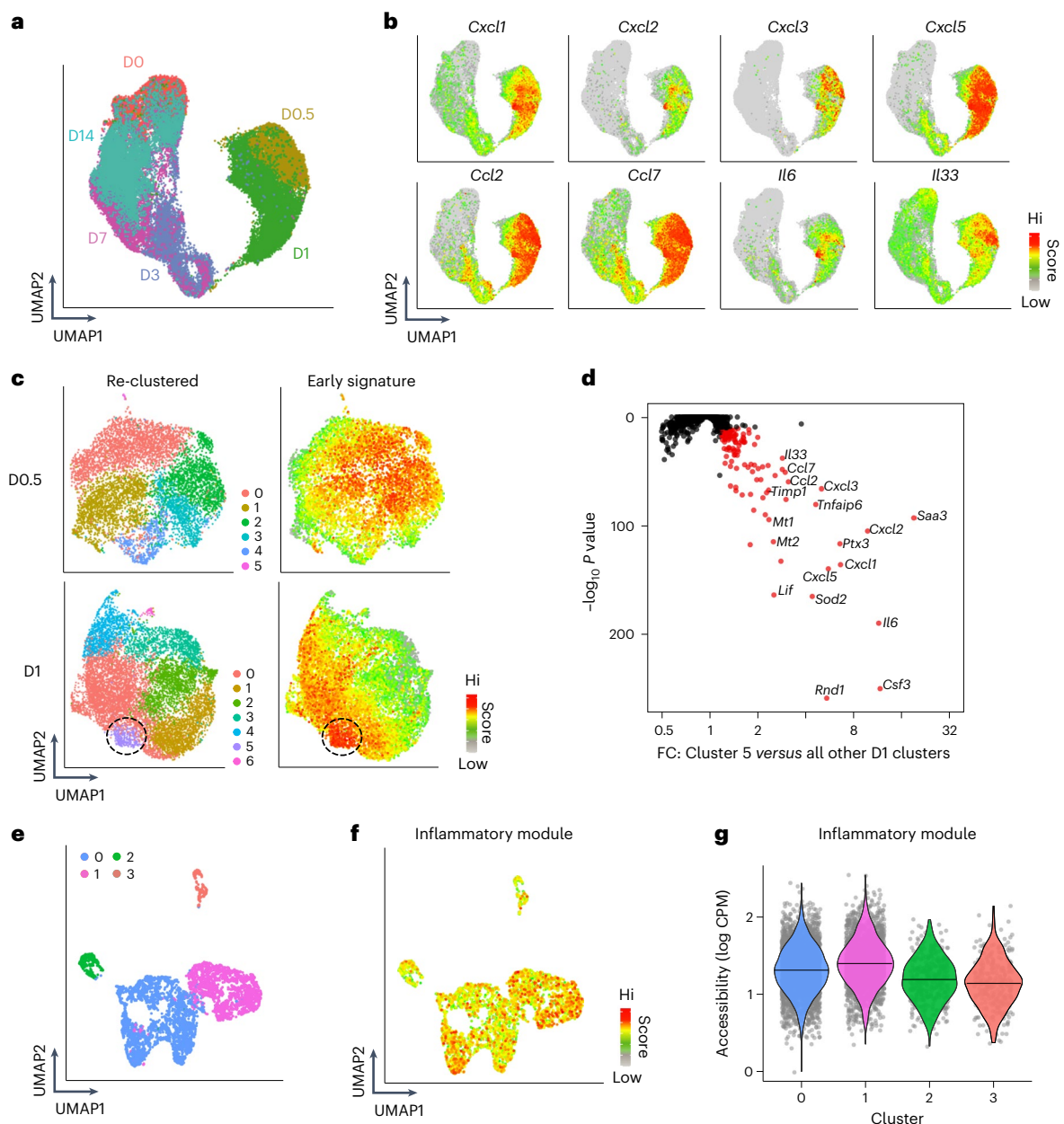


Fig. 1 | Identification of an inflammatory MmSC subtype after acute skeletal muscle injury. **a**, UMAP plot of MmSCs from hindlimb muscle of 6–8-week-old male *Foxp3*^{GFP} mice at homeostasis (D0) and 12 h (D0.5), 1 d (D1), 3 d (D3), 7 d (D7) and 14 d (D14) following CTX-induced injury. **b**, Same UMAP plot as in **a**, overlay with expression heat maps of the indicated transcripts. **c**, UMAP plot of re-clustered MmSCs from the D0.5 (top) and D1 (bottom) time points (left). Superimposition of a signature composed of the top 100 transcripts

distinguishing these early time points from the rest (right). **d**, P value versus fold change (FC) plot of the transcripts most differentially enriched in D1 cluster 5 compared to the other D1 clusters. **e**, UMAP of a public scATAC-seq dataset of muscle stromal cells at homeostasis⁴⁴. **f**, Same UMAP plot as in **e**, overlay with a signature score of the accessibility at loci encoding the top 100 differentially expressed transcripts from our D1 cluster 5. **g**, Violin plot of the signature score in **f** across clusters. CPM, counts per million.

and differentiation of the stem cells necessary for tissue regeneration^{7,21,23,30,35–37}. MmSCs are also responsible for the transient deposition of extracellular matrix that supports repair^{38–42}. Ablating MmSCs before acute injury results in a dramatic decrease in accumulation of CD45⁺ cells, suggesting an important immunomodulatory role^{21,22}, but the cellular and molecular underpinnings of this MmSC–immunocyte cross-talk remain largely unknown.

We exploited single-cell RNA sequencing (scRNA-seq) of MmSCs at key time points after acute injury to identify potential mediators of stromal cell–immunocyte communication; assessed their function in vivo using monoclonal antibody-driven depletions and MmSC transfers; and extended these findings to a muscular dystrophy model

of chronic muscle injury. The resulting data highlight the importance of an acutely induced ‘inflammatory’ MmSC subtype, which we also detected in other mouse and human mesenchymal stromal cell (mSC) compartments responding to a diversity of challenges.

Results

An inflammatory MmSC subtype emerges soon after acute injury

We performed scRNA-seq on MmSCs flow-cytometrically sorted from the hindlimb muscles (tibialis anterior, gastrocnemius and quadriceps) of 6–8-week-old B6.*Foxp3-Ires-Gfp* (*Foxp3*^{GFP}) male mice at homeostasis and at 0.5, 1, 3, 7 and 14 d after intramuscular (i.m.) injection of

cardiotoxin (CTX) (Extended Data Fig. 1a). A total of 44,231 high-quality cells were sequenced, encompassing an average of 7,372 cells per time point, with an average depth of 2,174 genes per cell. To obtain an overview of the regeneration time course, we merged and clustered the data from all time points. Visualization by Uniform Manifold Approximation and Projection (UMAP) revealed the cells to cluster largely according to the day post-injury (Fig. 1a). As expected, the day 14 (D14) cluster began to overlap with D0, indicating that the tissue was approaching homeostasis.

The D0.5 and D1 clusters cleanly separated from the cells of all the other time points. In assessing which transcripts drove this separation, we found by visual inspection, an enrichment for those encoding inflammatory mediators, in particular cytokines and chemokines (Fig. 1b). We then individually re-clustered the two earliest time points (D0.5 and D1) and superimposed a signature consisting of the top 100 transcripts distinguishing these time points from the rest (Fig. 1c). There was moderate dispersion at D0.5, but by D1, a distinct subpopulation highly enriched for this signature had emerged. Differential transcript analysis between this cluster (cluster 5, purple) and the rest of them revealed D1 cluster 5 cells to transcribe even more genes encoding inflammatory mediators (Fig. 1d and Extended Data Fig. 1b). Transcription of these genes was particularly low in clusters 2, 3, 4 and 6, which expressed markers of the previously described *Coll15a1*⁺ and *Pil6*⁺ steady-state mSC populations, proliferating mSCs and tenocytes, respectively (Extended Data Fig. 1b–d)^{43,44}.

Next, we addressed whether the bulk of MmSCs or just a specialized subtype had the potential to take on this inflammatory flavor. Scott et al. reported scRNA-seq and scATAC-seq data from muscle stromal cells at homeostasis⁴⁴. Employing *Hic1* as a stromal-cell marker, they identified four main clusters: two fibro-adipogenic, one tenogenic and one pericytic. Recapitulating these four clusters (Fig. 1e), we looked for increased accessibility at the loci encoding the top 100 transcripts differentially expressed by cluster 5 ('inflammatory signature') (Extended Data Table 1) in comparison with random, accessibility-matched loci. There was no strong enrichment of the inflammatory module among the various clusters (Fig. 1f,g). Similarly, superimposing on our dataset the transcripts encoded by differentially accessible loci in the four stromal subtypes from Scott et al. revealed no obvious correspondence between inflammatory cluster 5 and the steady-state stromal-cell subtypes (Extended Data Fig. 1e).

The inflammatory subtype is induced by a cytokine triplet

Pathway analyses on the 100-gene inflammatory signature revealed four major signaling pathways: interleukin (IL)-1, tumor necrosis factor (TNF)- α , oncostatin M (OSM) and IL-17 (Fig. 2a). We initially followed an in vivo gain-of-function approach to weigh the importance of these pathways. Just to set the parameters of the in vivo conditions, we intraperitoneally (i.p.) co-injected all four cytokines into uninjured mice and sorted MmSCs from the hindlimb muscles 2, 4 and 8 h later for population-level RNA-seq. There was a robust increase in the transcripts encoding many key inflammatory molecules, 2 h post-injection being the optimal time point to capture the inflammatory induction

(Extended Data Fig. 2a). We then repeated the experiment but injected the cytokines individually or as pairs. Volcano plots of each cytokine compared to the phosphate-buffered saline (PBS) control revealed that IL-1 β , TNF- α and OSM, but not IL-17A, strongly induced the inflammatory signature, with IL-1 β provoking the strongest response (Fig. 2b; note the differing *x* axes). Hierarchical clustering of the top 25 transcripts from the inflammatory signature across all conditions demonstrated that IL-1 β alone and IL-1 β plus OSM induced a set of transcripts most similar to that induced by the four cytokines together (Fig. 2c). Some discrete gene modules were also observed: one wherein transcripts were most highly expressed in the IL-1 β group, and two in which transcripts were more highly expressed by pairing OSM with IL-1 β over IL-1 β alone. Small gene modules also emerged among the other conditions. Thus, IL-1 β , TNF- α and OSM induced a complex signaling network within MmSCs, invoking additive, discordant or redundant responses.

Population-level RNA-seq on the four major muscle cell compartments at homeostasis and on D1 after CTX-induced injury revealed that the CD45⁺ compartment was the sole expressor of transcripts encoding these cytokines (Fig. 2d). To examine their expression among hematopoietic-lineage cells, we took advantage of a scRNA-seq dataset from Oprescu et al. depicting whole hindlimb muscle at various time points after CTX-induced injury¹⁶. Re-analysis of the earliest time point, D0.5, demonstrated that MFs, monocytes (MOs) and NFs expressed the most *Il1b*, *Tnf* and *Osm* transcripts (Extended Data Fig. 2b). (There was only low expression of the three cytokines in muscle cells, themselves.) We also employed flow cytometry to quantify IL-1 β and TNF- α levels in uninjured hindlimb muscle and at 15 and 60 min post-CTX (Fig. 2e and Extended Data Fig. 2c). (There are no commercially available antibodies suitable for cytofluorimetric quantification of OSM levels.) MOs, followed by dendritic cells, were the most abundant and rapidly accumulating IL-1 β -producing populations (Fig. 2f). (Here and subsequently, we use fraction of live cells as a surrogate for cell numbers to correct for extraction efficiencies, which can be variable with such tissue preps.) MFs and MOs were the most abundant TNF- α ⁺ cells (Fig. 2f).

Myeloid cells are dispensable for the inflammatory subtype

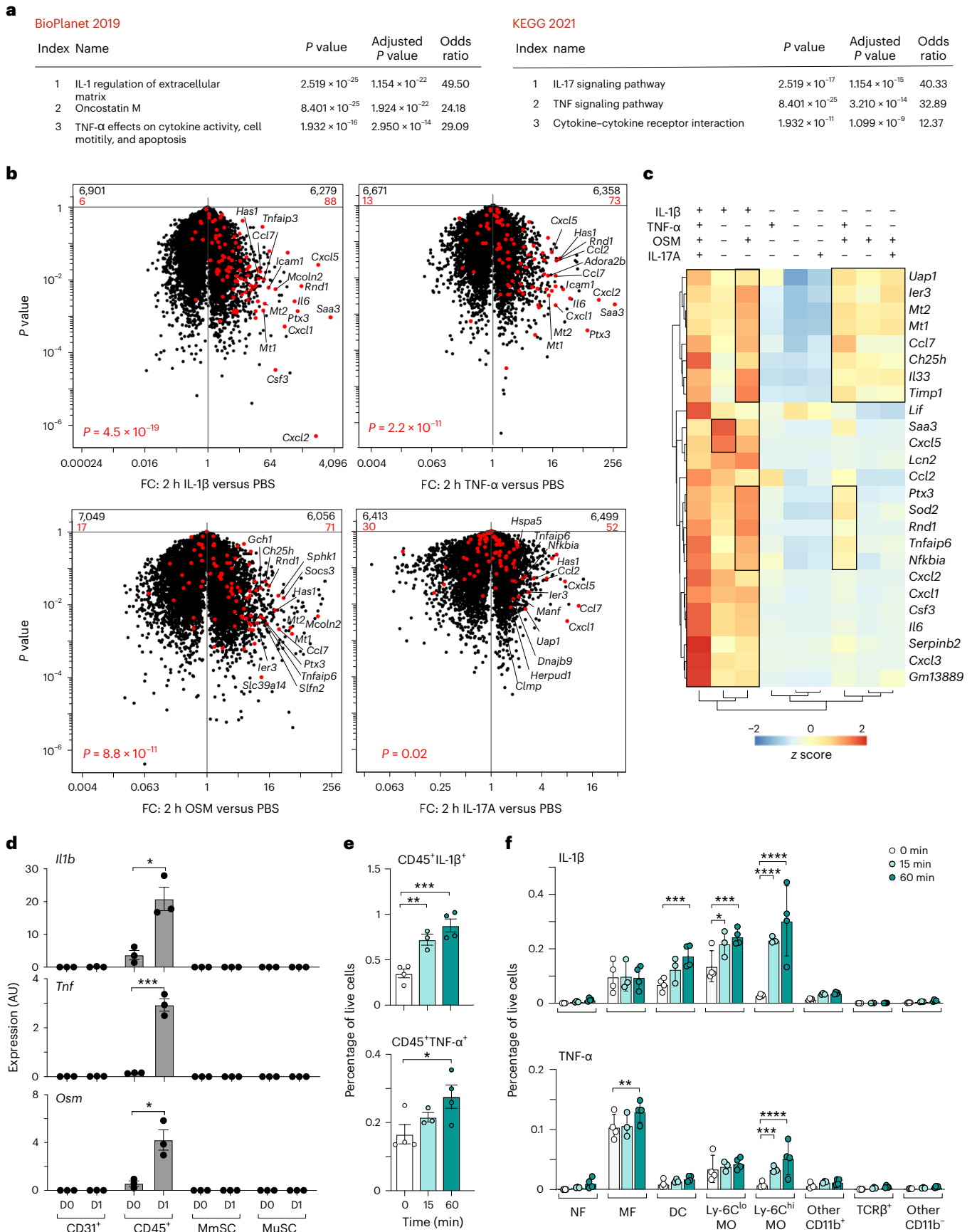
Myeloid cells, primarily NFs followed by MFs, are usually the earliest arrivals in damaged tissues, and their role in activating stromal cells has been described^{45,46}. Thus, we addressed whether induction of the inflammatory MmSC subtype was strictly dependent on soluble factors derived from myeloid cells.

Some initial observations argued for a different scenario. First, loss of IL-1 β alone did not substantially alter induction of the inflammatory MmSC program (Extended Data Fig. 3a); moreover, this module was only mildly decreased by antibody-mediated co-neutralization of IL-1 β , TNF- α and OSM (Extended Data Fig. 3b).

To formally address the contribution of NFs and MFs in MmSC acquisition of the inflammatory program, we depleted NFs with anti-Ly-6G monoclonal antibody or MFs by diphtheria toxin (DT) administration to *Lysm*^{Cre} *XCsf1*^{LSL-DTR} mice⁴⁷, and assessed the inflammatory signature in MmSCs 12 h after CTX-induced injury (to avoid

Fig. 2 | IL-1 β , TNF- α and OSM produced by myeloid cells strongly induce the inflammatory MmSC subtype. **a**, Pathway analyses of the 100-gene inflammatory signature. **b**, Volcano plot comparisons of MmSCs after injections of IL-1 β versus PBS (top, left), TNF- α versus PBS (top, right), OSM versus PBS (bottom, left) or IL-17A versus PBS (bottom, right). The 100-gene inflammatory signature is shown in red, with the numbers at the top of each plot indicating numbers of up- and downregulated transcripts (in comparison with total transcript numbers in black). **c**, Hierarchically clustered heat map of the top 25 transcripts in the inflammatory signature across the cytokine augmentation conditions. **d**, Expression of inflammatory MmSC-inducing transcripts across the major skeletal-muscle-cell compartments at homeostasis (D0) and on D1 after CTX-induced injury. Cytofluorimetrically sorted cells were subject to

RNA-seq ($n = 3$ mice per time point). **e, f**, Cytofluorimetric analysis of IL-1 β and TNF- α levels in CD45⁺ cells in uninjured hindlimb muscle and at 15 and 60 min post-CTX injection ($n = 4$ mice per time point). Note, one sample was removed from the 15 min group as it was $3 \times$ s.d. from the mean. Total CD45⁺IL-1 β ⁺ (top) and CD45⁺TNF- α ⁺ (bottom) cells (**e**). Distribution of IL-1 β ⁺ (top) and TNF- α ⁺ (bottom) cells (**f**). Cytofluorimetric data were pooled from two independent experiments. Data are from 7–9-week-old B6 male mice. AU, arbitrary units; DC, dendritic cell; MO, monocyte. Plots with error bars displayed as mean \pm s.e.m. * $P < 0.05$, ** $P < 0.01$, *** $P < 0.001$, **** $P < 0.0001$. A one-sided Fisher's exact test with and without correction by the Benjamini–Hochberg method (**a**), chi-squared test (**b**), two-tailed unpaired *t*-test (**d**), one-way analysis of variance (ANOVA) (**e**) and two-way ANOVA with Dunnett's multiple comparisons test (**f**) were used for analysis.



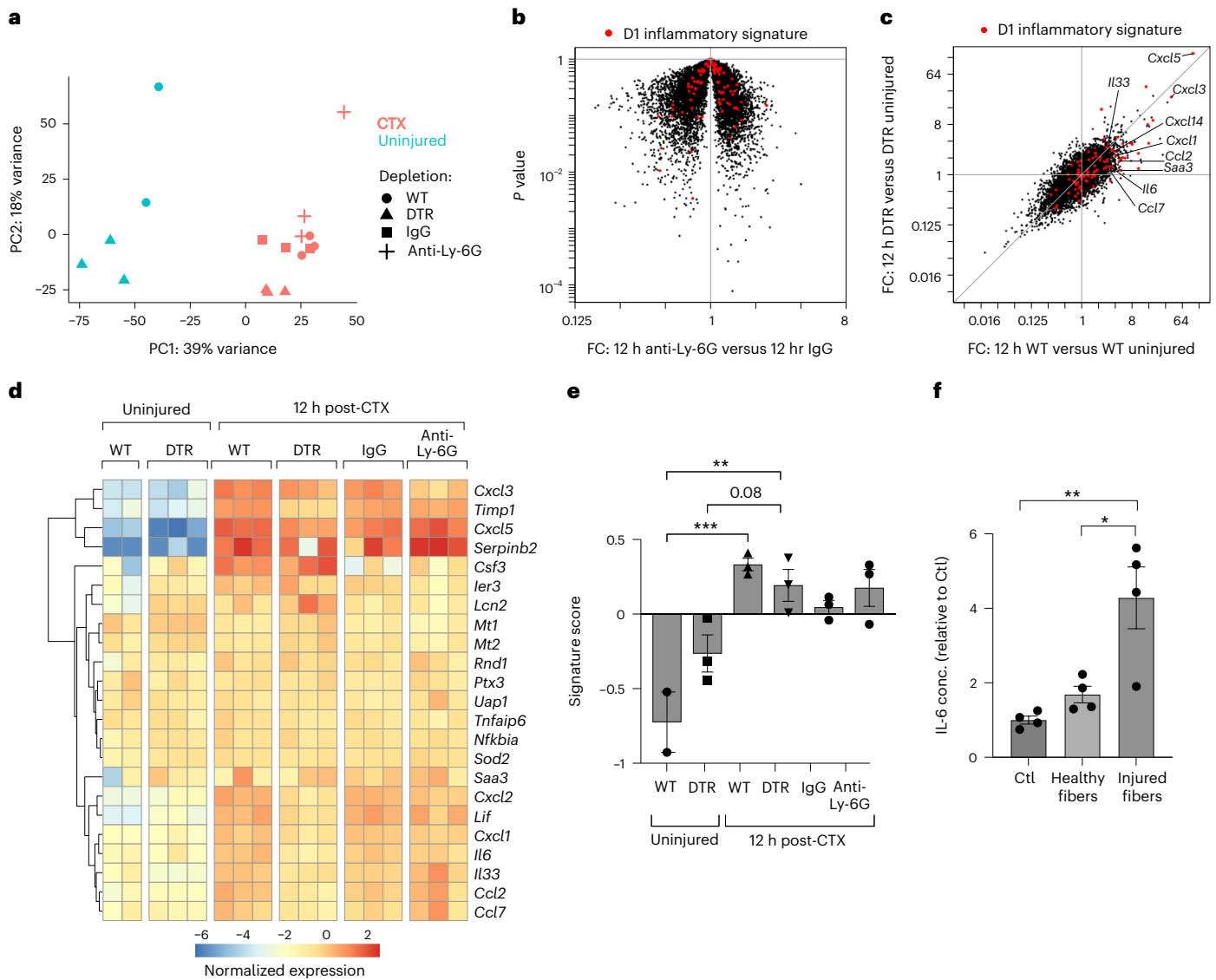


Fig. 3 | Induction of the inflammatory MmSC subtype is not strictly dependent on myeloid cells. a–e, RNA-seq analysis of cytofluorimetrically sorted MmSCs from uninjured and CTX-injured mice ($n = 2–3$ mice per group). PCA (a). Volcano plot comparisons of MmSCs from B6 male mice treated with anti-Ly-6G versus IgG isotype control (b). The 100-gene inflammatory signature is shown in red. Transcriptomic FC/FC plot of MmSCs from CTX-injured versus uninjured *Lysm^{wt} X Csf1r^{sl-DTR}* (WT, macrophage-containing) mice (x axis) vis-a-vis CTX-injured versus uninjured *Lysm^{cre} X Csf1r^{sl-DTR}* (DTR, macrophage-depleted) mice (y axis) (c). The 100-gene inflammatory signature is shown in red. Hierarchically clustered heat map of the top 25 transcripts in the inflammatory

signature across the different conditions (d). Signature score of the 100-gene inflammatory MmSC gene set (e). Scores were calculated as shown in the Methods. f, Freshly isolated MmSCs were cultured alone (Ctl) or co-cultured with muscle fibers that were pre-treated either with vehicle (healthy fibers) or CTX (injured fibers) and IL-6 levels in the culture supernatants were determined by ELISA (two independent experiments). Data are from 7–9-week-old male mice. DTR, DT receptor. Plots with error bars are displayed as mean \pm s.e.m. * $P < 0.05$, ** $P < 0.01$, *** $P < 0.001$. A chi-squared test (b) and one-way ANOVA with Tukey’s multiple comparisons test (e,f) were used for analysis.

secondary effects) by population-level RNA-seq. Principal-component analysis (PCA) showed that the injury status contributed the largest principal component, followed by the effect of MF depletion (Fig. 3a); NF depletion had no impact on the MmSC inflammatory program (Fig. 3b). MF-depleted mice still upregulated the inflammatory module, but to a lower degree than did their MF-containing counterparts, as evidenced by the off-diagonal cloud on the fold change/fold change plot of Fig. 3c. Transcripts encoding some components of the inflammatory program were reduced in the absence of MFs (such as *Il6* and *Cxcl2*) while others were not affected (such as *Cxcl5* and *Cxcl3*) (Fig. 3d). We also calculated a signature score for the inflammatory gene set, and observed only a mild attenuation of this program after MF depletion (Fig. 3e), suggesting that MFs might amplify the inflammatory program,

but were dispensable for MmSC activation, at least at this early time point post-injury.

These data raised the possibility that MmSCs could sense muscle damage independently of myeloid cell input. To address this possibility, we sorted MmSCs from uninjured mice and co-cultured them with single muscle fibers pre-treated with either vehicle or CTX. As a measure of MmSC activation, we quantified IL-6 levels in the supernatant after 24 h. CTX-injured, but not healthy, muscle fibers induced a higher level of IL-6 in the supernatant (Fig. 3f). Thus, parenchymal damage and, potentially, signals from other non-myeloid cells could trigger induction of the MmSC inflammatory subtype, a process further amplified by multiple cytokines derived from myeloid cells acting in a redundant manner.

Isolated inflammatory MmSCs induce inflammation

We then attempted to identify cell-surface markers that would permit cytofluorimetric discrimination of inflammatory MmSCs from other MmSCs. Among the transcripts enriched in the inflammatory subtype, there were only a few that encoded surface markers, and these proved useless for cytofluorimetric distinction. Instead, we generated a new line of reporter mice. According to our scRNA-seq dataset, *Il6* expression was highly specific to the inflammatory subtype (Extended Data Fig. 4a). Re-analysis of the scRNA-seq dataset from Oprescu et al. confirmed that *Il6* was induced in stromal cells only following injury (Extended Data Fig. 4b). Recently, Heink et al. developed an IL-6 reporter/deleter mouse line (*Il6*^{tm3307(Cerulean-P2A-CD90.1)Arte}, abbreviated as *Il6*RD), which, when crossed with a Cre line, allows for the coupling of *Thy1.1* and *Il6* expression in a designated population of cells⁴⁸. The *Il6*RD line is carried on a Thy1.2⁺ genetic background, making *Il6*-expressing cells the only ones that are Thy1.1⁺. We crossed the *Il6*RD line with the C57BL/6-*Tg(Pdgfra-Cre)1Clc/J* (*Pdgfra-Cre*) line and profiled Thy1.1 expression across the major muscle cell compartments at homeostasis and 12 h after CTX injury, the first time point at which we had identified inflammatory transcripts in MmSCs by scRNA-seq. There was minimal Thy1.1 expression at steady state, consistent with low baseline *Il6* expression in the muscle (Extended Data Fig. 4b). A Thy1.1⁺ MmSC population emerged at 12 h, whereas there was low signal across the other compartments (Fig. 4a). To confirm that Thy1.1⁺ MmSCs were enriched in inflammatory transcripts, we isolated Thy1.1⁺ and Thy1.1⁻ MmSCs 12 h following CTX injury and performed population-level RNA-seq. Indeed, Thy1.1⁺ cells were significantly enriched in the inflammatory MmSC program (Fig. 4b).

We first used this system to investigate the spatial distribution of inflammatory MmSCs. Confocal imaging of injured muscles from *Il6*RD × *Pdgfra-Cre* mice showed that Thy1.1⁺PDGFRα⁺ MmSCs localized to areas of high NF infiltration and muscle fiber damage (Fig. 4c).

To determine whether isolated inflammatory MmSCs could induce inflammation in muscle tissue, we prepared Thy1.1⁺ and Thy1.1⁻ MmSCs from hindlimb muscles 2 and 4 d after CTX injury, respectively and i.m. injected them into uninjured hindlimb muscles (Fig. 4d). Thy1.1⁺ MmSCs were isolated on D2 because the MmSC population expands with injury, allowing for more cells to be collected; Thy1.1⁻ MmSCs were isolated on D4 because some of these cells could convert to Thy1.1⁺ MmSCs during the earliest stages of muscle injury, whereas on D4 their inflammatory potential was minimal. We transferred the MmSCs into B6.Cg-*Tg(CAG-tdKaede)1Sutr* (Kaede) mice, a line in which all cells express Kaede, a green fluorescent reporter. By 16 h after transfer, Kaede-negative donor cells were readily identified in the hindlimb muscle of the recipient mice (Fig. 4e,f). Mice harboring Thy1.1⁺ cells showed a significant increase in CD45⁺ hematopoietic-lineage cells vis-a-vis those receiving Thy1.1⁻ cells (Fig. 4g). Within the CD45⁺ compartment, NFs and Ly-6C^{hi} MFs, key innate immunocytes in the early response to muscle injury, were specifically increased in mice that received Thy1.1⁺ MmSCs (Fig. 4h,i).

CXCL5 non-redundantly promotes the influx of NFs

As Thy1.1⁺ MmSCs proved resistant to conventional (monoclonal antibody-driven) depletions, we took up a candidate mediator

approach, favoring transcripts that (1) were part of the inflammatory MmSC signature; (2) were enriched in stroma relative to the other major muscle cell compartments; and (3) were induced by injury. *Cxcl5* emerged as the strongest candidate as it was one of the most differentially expressed transcripts in the inflammatory MmSC subtype, was strongly enriched in the stroma and was the most highly induced MmSC transcript upon injury, with a fold change >2,500 (Fig. 5a–c and Extended Data Fig. 4c). Re-analysis of the scRNA-seq dataset from Oprescu et al. confirmed that *Cxcl5* transcripts were not made at homeostasis, but upon injury were highly enriched in stromal cells at 0.5 d and 2 d following injury (Extended Data Fig. 4d). CXCL5 is primarily known as a chemoattractant for NFs and can regulate the levels of other chemokines, such as CXCL1 and CXCL2 (ref. 49). During acute skeletal muscle injury, NFs at early stages of injury are important for removing cellular debris to permit effective tissue repair^{9,50,51}. Furthermore, following myocardial infarction, NFs in the heart actively secrete factors that help polarize MFs to a pro-reparative phenotype⁵². To investigate the role of CXCL5 during skeletal muscle injury, we administered anti-CXCL5 monoclonal antibody before and coincident with i.m. injection of CTX. At 24 h after injury, there was no change in total CD45⁺ hematopoietic-lineage cells; however, there was a decrease in the percent of NFs, suggesting that CXCL5 was a non-redundant NF chemoattractant during muscle injury (Fig. 5d,e). While there was no evident change in MF numbers, there were, notably, significant increases in the representation of adaptive immunocyte populations such as T and B cells (Fig. 5f–h). This increase was recapitulated by depleting NFs with anti-Ly-6G monoclonal antibody, also administered before and coincident with i.m. injection of CTX (Fig. 5j,l,m). Total CD45⁺ hematopoietic-lineage cell numbers were unaffected; however, MF numbers were elevated in the treatment group (Fig. 5i,k).

Early loss of CXCL5 prolongs inflammation and inhibits repair

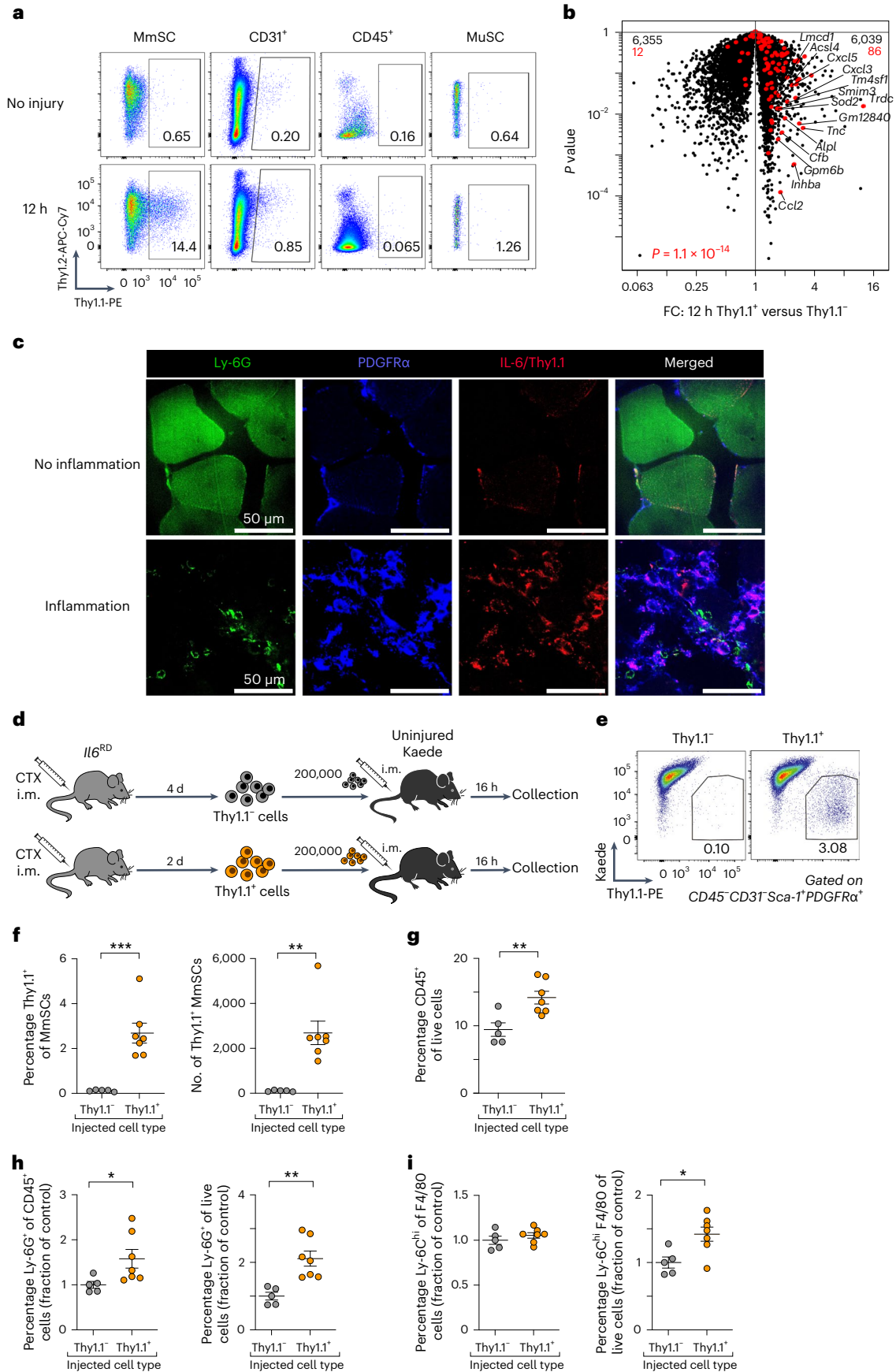
We neutralized CXCL5 during the earliest stage of recovery after CTX-induced injury (D-0.5, D0, D1 and D2) and analyzed hindlimb muscle at D7 by flow cytometry, whole-tissue RNA-seq and histology. There was no difference in the accumulation of CD45⁺ hematopoietic-lineage cells, but NFs and pro-inflammatory Ly-6C^{hi} MFs were elevated in the anti-CXCL5-treated, compared to the IgG-treated, group (Fig. 6a–c). At D7, the levels of these innate immunocyte populations are usually very low as they are key elements of the early inflammatory stage of the injury response but not the later reparative stage^{15,16}. Thus, elevated numbers of these immunocytes at D7 points to aberrantly persistent inflammation.

Whole-tissue RNA-seq data aligned with these findings. Aguilar et al. recently published highly useful gene sets that define key pathways in skeletal muscle recovering from acute injury⁵³. We calculated signature scores based on the expression of these gene sets to identify pathways that varied in the presence and absence of anti-CXCL5 treatment. There were distinct increases in the ‘inflammation’ and ‘pro- to anti-inflammatory’ pathways in the anti-CXCL5-treated group (Fig. 6d). Subcategories within the ‘pro- to anti-inflammatory’ pathway revealed more specific enrichments in ‘phagocytic and complement

Fig. 4 | Transfer of inflammatory MmSCs can induce inflammation.

a, Cytofluorimetric quantification of Thy1.1 expression across the major skeletal-muscle-cell compartments in *Il6*RD × *Pdgfra-Cre* mice at homeostasis and 12 h following CTX-induced injury. **b**, Volcano plot comparison of transcripts expressed by Thy1.1⁺ and Thy1.1⁻ MmSCs 12 h after CTX injection ($n = 3$). The 100-gene inflammatory signature is shown in red; numbers at the top indicate up- and downregulated transcripts (in comparison with total transcript numbers in black). **c**, Immunofluorescence imaging of the indicated markers in muscle sections of *Il6*RD × *Pdgfra-Cre* mice 2 d following CTX-induced injury (×60 magnification). Representative images of areas with no NF infiltration (no inflammation) (top). Representative images of areas with high NF infiltration

(inflammation) (bottom). Experiment repeated twice with similar results. **d**, Schematic of the adoptive-transfer design used to generate the data in e–i. **e–i**, Cytofluorimetric profiling of cells from hindlimb muscles of recipient mice following Thy1.1⁺ ($n = 7$) versus Thy1.1⁻ ($n = 5$) MmSC transfer. Representative flow plots (**e**); summary quantification of Thy1.1⁺ cells (**f**); and quantification of CD45⁺ cells (**g**), NFs (**h**) and Ly-6C^{hi} MFs (**i**). Transfer data were pooled from two independent experiments. Each data point represents an individual mouse within a group. All data are from 7–9-week-old male mice. Plots with error bars are displayed as mean ± s.e.m. * $P < 0.05$, ** $P < 0.01$, *** $P < 0.001$. Data were analyzed by a two-tailed unpaired *t*-test except for **b**, in which a chi-squared test was performed.



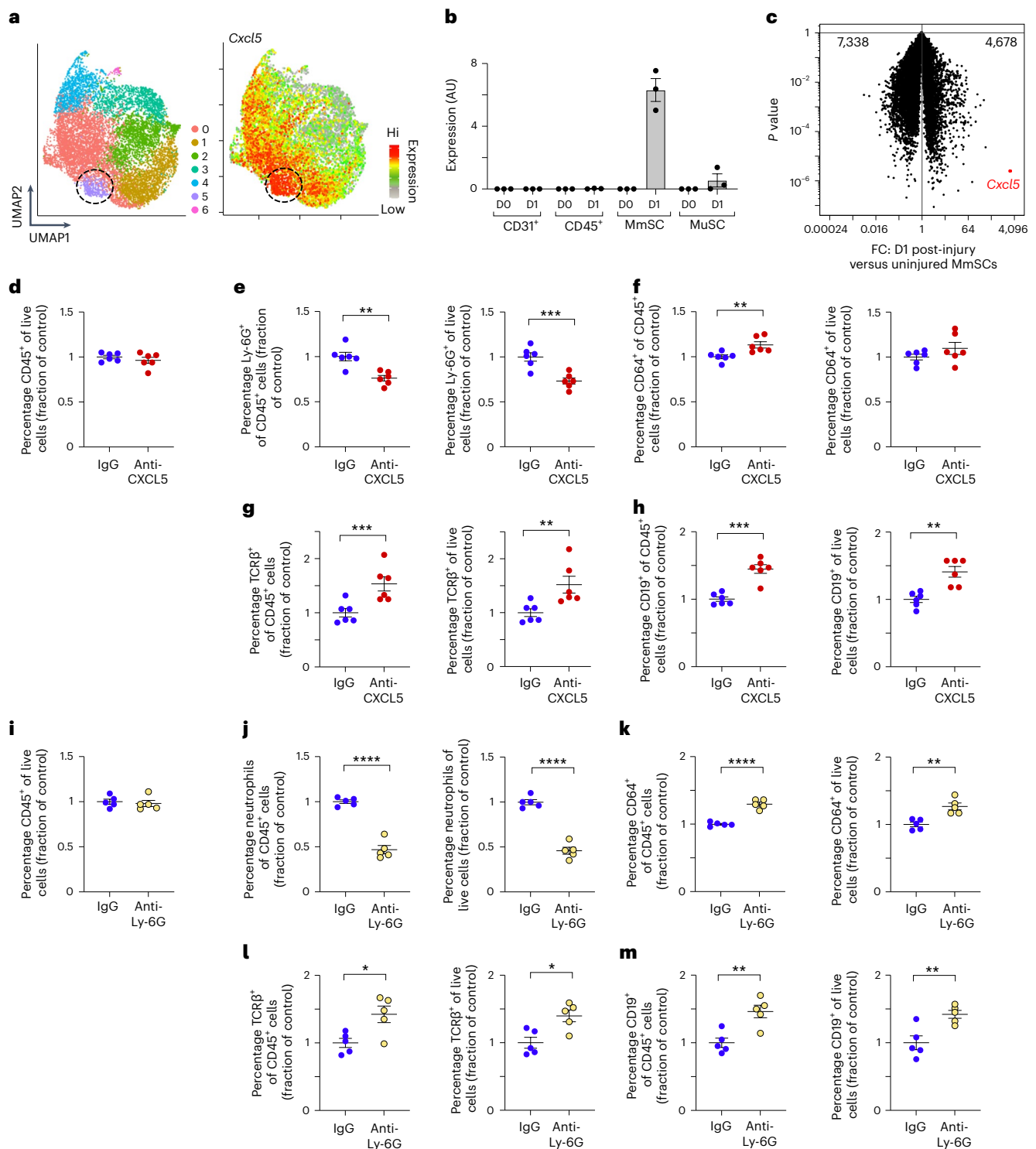


Fig. 5 | CXCL5 is a stroma-specific chemokine that promotes NF influx following CTX-induced injury. **a**, UMAP plot of MmSCs from D1 following CTX-induced injury (left) overlain with a heat map of *Cxcl5* expression (right). **b**, *Cxcl5* expression across the major skeletal-muscle-cell compartments at homeostasis (D0) and on D1 after CTX-induced injury ($n = 3$ mice per time point). **c**, Volcano plot comparison of D0 versus D1 MmSCs ($n = 3$ mice per time point). *Cxcl5* is highlighted in red. Numbers at the top indicate total genes up- and downregulated in response to injury. **d–h**, Anti-CXCL5 monoclonal antibody or IgG was administered 12 h before and coincident with CTX injection, and cells from hindlimb muscles were cytofluorimetrically profiled one day after injury ($n = 6$ per group). Quantification of (**d**) total CD45⁺ cells, (**e**) NFs, (**f**) MFs, (**g**) $\alpha\beta$ T cells and (**h**) B cells. **i–m**, Anti-Ly-6G monoclonal antibody or IgG was

administered 2 d, 1 d and coincident with CTX injection, and cells from hindlimb muscles were cytofluorimetrically profiled 1 d after injury ($n = 5$ per group). Quantification of total CD45⁺ cells (**i**), NFs (**j**), MFs (**k**), $\alpha\beta$ T cells (**l**) and B cells (**m**). As the depleting antibody covered the Ly-6G epitope, NFs were defined as CD45⁺CD11b⁺CD64⁺CD11c⁺Ly-6C⁺GR-1⁺. Antibody-mediated depletion data were pooled from two independent experiments. Besides **a** and **c**, each data point represents an individual mouse within a group. All, except the scRNA-seq, data derived from 7–9-week-old B6 male mice. Plots with error bars displayed as mean \pm s.e.m. * $P < 0.05$, ** $P < 0.01$, *** $P < 0.001$, **** $P < 0.0001$ by a two-tailed unpaired *t*-test. Data were normalized to the IgG group as repeated experiments had different control set points.

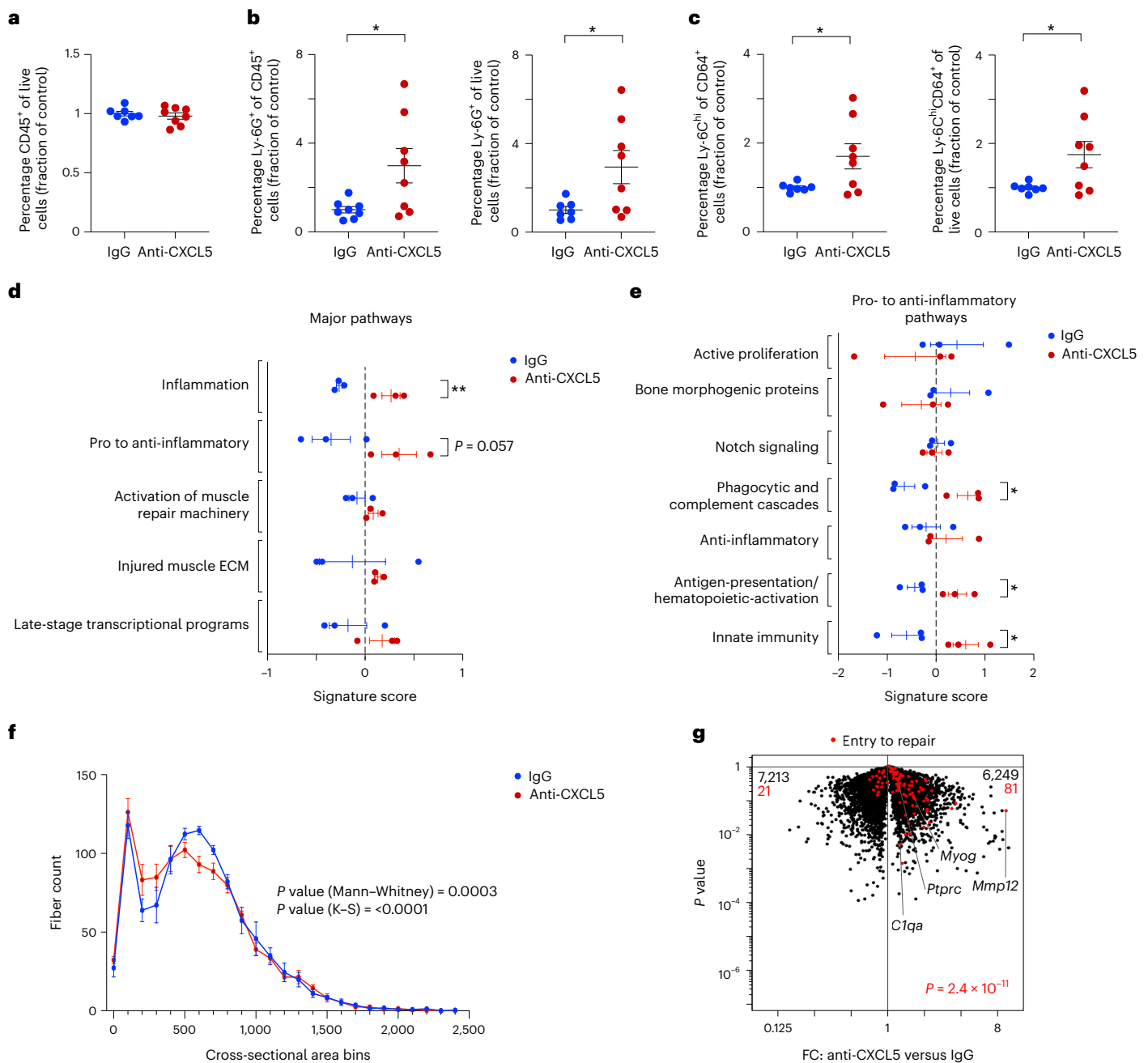


Fig. 6 | CXCL5 is necessary for effective tissue repair. Anti-CXCL5 monoclonal antibody ($n = 8$) or control IgG ($n = 7$) was injected during the earliest stage of recovery after CTX injury (D-0.5, D0, D1 and D2) and at D7, hindlimb muscle was profiled by cytofluorimetry. **a**, Total CD45⁺ cells. **b**, NFs. **c**, Ly-6C^{hi} MFs. **d,e**, Transcriptional analyses of whole muscle tissue at D7 ($n = 3$ mice per condition). Signature scores of major (**d**) and pro- to anti-inflammatory (**e**) pathways⁵³. Scores were calculated as described in the Methods. **f**, Histogram of the cross-sectional areas of centrally nucleated muscle fibers at D7 ($n = 5$ mice per condition). **g**, Volcano plot comparing whole-muscle transcripts

from anti-Cxcl5-treated and control-IgG-treated mice overlain with a signature of genes ordinarily shut down during the transition from inflammation to repair¹⁸. Except for **f** and **g**, each data point represents an individual mouse within a group. All data were from 7–9-week-old B6 male mice. Plots with error bars are displayed as mean \pm s.e.m. * $P < 0.05$, ** $P < 0.01$ by a two-tailed unpaired t -test except for **f**, in which two-tailed Mann–Whitney and Kolmogorov–Smirnov (K–S) tests were performed, and **g** in which a chi-squared test was performed. Data were normalized to the IgG group as repeated experiments had different control set points.

cascades; ‘antigen presentation/hematopoietic activation’ and ‘innate immunity’ (Fig. 6e).

Last, we assessed the impact of anti-CXCL5 treatment on muscle regeneration, quantifying the cross-sectional areas of 1,000 representative muscle fibers per mouse on hematoxylin and eosin (H&E)-stained tissue sections. Administration of anti-CXCL5 resulted in a profile of cross-sectional areas shifted toward smaller values in comparison with those observed with injections of IgG, which was an indication of

less-mature muscle fibers and therefore, a defect or slowdown in the regeneration process (Fig. 6f). Moreover, overlaying an ‘entry to repair’ signature¹⁸ on a volcano plot of whole-muscle transcripts showed that anti-CXCL5-treated mice did not downregulate this program as control mice do, for example, key transcripts such as *C1qa*, *Mmp12* and *Ptpcr* (Fig. 6g). Given that the early inflammatory MmSC subtype was the primary expressor of *Cxcl5* transcripts, these observations argue for the importance of this stromal element.

Inflammatory MmSCs occur in a model of muscular dystrophy

To extend these findings to chronic injury, we performed scRNA-seq on MmSCs isolated from a mouse model of Duchenne's muscular dystrophy (DMD), D2.B10 *Dmd*^{mdx} (*mdx*), compared to its control line, DBA/2J (CTL). DMD is an X-linked disease caused by a mutation in the dystrophin gene. Without functional dystrophin, the structural integrity and contractile activity of skeletal muscle is compromised, leading to repetitive injury and ultimately the replacement of muscle tissue with fibrosis and fat.

We isolated MmSCs from the hindlimb muscles of 2.5-, 5- and 12.5-week-old *mdx* mice, and from 2.5- and 12.5-week-old CTL mice, time points chosen to survey the onset and early progression of the disease process. Then, 13,650 cells were sequenced, with an average of 2,730 cells per condition and an average depth of 2,686 genes per cell. We initially clustered cells from *mdx* mice only. UMAP visualization revealed the time points to cluster predominantly separately, indicating that MmSCs changed dramatically as the disease progressed, even over a mere 10-week span (Fig. 7a). Notably, by overlaying on the UMAP plot the inflammatory signature derived from CTX-induced muscle injury (top 100 genes defining the inflammatory MmSC subtype; referred to as the 'CTX-inflammatory signature') (Extended Data Table 1), we could distill a small group of cells enriched for this inflammatory module. These cells were members of cluster 5 (light blue), composed mainly of MmSCs from the 5 and 12.5-week time points, indicating that cells turned this program on at an early age, though primarily after weaning.

We then co-clustered MmSCs from 2.5-week-old *mdx* and CTL mice ('early time point'). Cells from both genotypes were distributed across all of the clusters (Fig. 7b). Density plots highlighting areas on the UMAP plot enriched for a particular genotype indicated that, while there were some minor condition-specific areas, cells from the two genotypes primarily overlapped. In contrast, cells from 12.5-week-old *mdx* and CTL mice ('late time point') primarily did not overlap (Fig. 7c). Thus, as disease progressed, *mdx* MmSCs acquired a transcriptome largely distinct from that of baseline MmSCs. We next imposed the CTX-inflammatory signature on the early and late UMAP plots: at the early time point, the signature score was low across all clusters (Fig. 7d), but later, cluster 4 (light blue) emerged with an elevated signature score (Fig. 7e). Cluster 4 was unique to the *mdx* condition. These data reveal that the inflammatory MmSC subtype indeed (1) was present in a chronic muscle-injury model; (2) emerged as the disease progressed; and (3) was disease-specific.

While single-cell datasets are helpful for understanding cellular heterogeneity, their lack of depth can compromise accurate determination of gene expression. Therefore, we performed population-level RNA-seq on double-sorted MmSCs from *mdx* mice at 2.5, 7 and 12.5 weeks of age. Given that MmSCs from the *mdx* and CTL genotypes were transcriptionally similar at 2.5 weeks, we used this time point as our primary reference. Superimposition of the CTX-inflammatory signature on a volcano plot comparing MmSCs from 7 and 2.5 weeks demonstrated a significant enrichment in the MmSCs of 7-week-old mice (Fig. 7f). Numerous signature transcripts were highly upregulated, notably *Cxcl5*. A comparison of MmSCs from 12- and 2.5-week-old mice revealed a persistent enrichment of the CTX-inflammatory signature at this later stage, albeit with slightly lower transcript fold changes (Fig. 7g).

Pathway analyses of genes that were twofold enriched, at either the 7-week (1,239 genes) or 12.5-week (701 genes) compared to the 2.5-week time point, indicated that most of the top pathways enriched at 7 weeks were, not surprisingly, related to inflammation and cell cycle (Fig. 7h), whereas those enriched at 12.5 weeks were similarly related to inflammation, but with an additional prominence of complement terms (Fig. 7i).

Inflammatory MmSCs occur in diverse tissues and pathologies

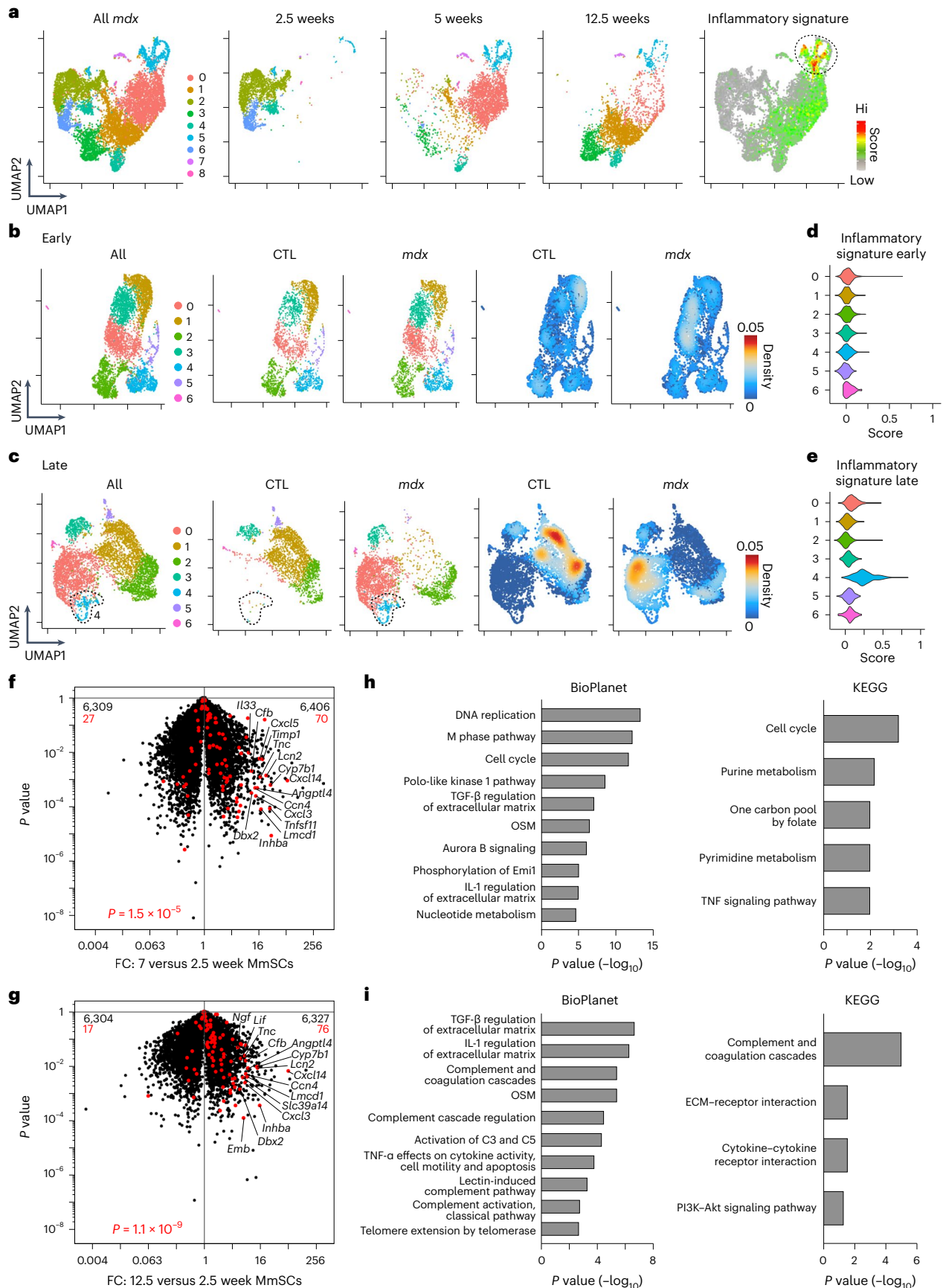
We exploited previously published data to determine whether an inflammatory MmSC subtype could be found in other tissues, either at homeostasis or with perturbation. Given the similarities between skeletal and cardiac muscle, we began by analyzing a scRNA-seq dataset from mouse heart tissue at homeostasis (D0) and at numerous time points (D1, D3, D5, D7, D14 and D28) following myocardial infarction (MI)⁵⁴. At each time point, cardiomyocytes, debris and dead cells were removed and the remaining cells were captured and sequenced. We clustered these cells, extracted the *Pdgfra*⁺ clusters, re-clustered them and visualized the new clusters on a UMAP plot, both in toto and day by day (Fig. 8a). To search for the inflammatory module across tissues and to reduce contributions that might be intrinsic to the skeletal muscle environment, we created a condensed inflammatory signature using only the top 25 genes from the 100-gene CTX-inflammatory signature (Extended Data Table 1). A few focal areas with high signature scores (encircled) emerged (Fig. 8b). D1 *Pdgfra*⁺ cells were clearly most enriched in these regions of the UMAP plot. With time following injury, the signature score was attenuated. Violin and dot-plots of the signature score across the time points confirmed these findings (Fig. 8c,d). In contrast, at both homeostasis and the latest stages of recovery from injury (D14 and D28), the signature scores were very low.

A mouse scRNA-seq dataset from podoplanin (PDPN)⁺ stromal cells derived from a pancreatic ductal adenocarcinoma model was analyzed next⁵⁵. CD45⁺ Epcam⁻ CD24a⁻ CD31⁻ PDPN⁺ cells were isolated from healthy pancreas tissue, tumor-adjacent tissue and small (1–4 mm) and large (5–10 mm) tumors. We clustered these cells, extracted *Pdgfra*⁺ clusters, re-clustered them and visualized them together and by condition (Fig. 8e). Superimposing the 25-gene CTX-inflammatory signature on the UMAP plot highlighted a discrete area with a high signature score (Fig. 8f). At homeostasis (WT) there was no appreciable signature detection (Fig. 8g,h); however, in the sequence of tumor progression, the signature score became elevated in tumor-adjacent samples, peaked in small-tumor samples and then was reduced in large-tumor samples.

Two murine models of auto-inflammatory disease were also examined. In one case, a scRNA-seq dataset covering CD45⁺ synovial cells from the inflamed joints of a model of rheumatoid arthritis (RA) was analyzed⁵⁶. We clustered all of the cells in the dataset, extracted the *Pdgfra*⁺ clusters, re-clustered them and visualized the data on a UMAP plot. Overlaying the 25-gene CTX-inflammatory signature highlighted a focal region with enriched signal (Fig. 8i). In the second case, we similarly analyzed a scRNA-seq dataset from CD45⁺ Epcam⁻ cells isolated from colons of healthy or dextran sodium sulfate-treated mice, a model of inflammatory bowel disease⁵⁷. Low signature scores were observed in cells originating from healthy colons while those from mice with colitis showed specific areas of enrichment (Fig. 8j).

Fig. 7 | Identification of an inflammatory MmSC subtype in a mouse model of muscular dystrophy. a–e, scRNA-seq of MmSCs from 2.5-, 5- and 12.5-week-old *mdx* mice, and from 2.5- and 12.5-week-old CTL mice. UMAP plots of all cells from *mdx* mice (left-most), cells from each time point (three middle panels) and cells superimposed with the 100-gene CTX-inflammatory signature (right-most) (a). UMAP plots of *mdx* and CTL cells from 2.5-week-old mice ('early') (b) and from 12.5-week-old mice ('late') (c). Both genotypes (left); individual genotypes (middle); and density plots of individual genotypes (right). Violin plots of the CTX-inflammatory signature for the 'early' (d) and 'late' (e) clusters.

f–i, Population-level RNA-seq of MmSCs from 2.5-, 7- and 12.5-week-old *mdx* mice. Volcano plot comparisons of MmSCs from 7-week-old versus 2.5-week-old (f) and 12.5-week-old versus 2.5-week-old (g) mice ($n = 3$ per time point). The 100-gene inflammatory signature is shown in red; numbers at the top indicate up- and downregulated transcripts (in comparison with total transcript numbers in black). Pathway analyses of transcripts significantly upregulated ($>2\times$, $P < 0.05$) in MmSCs from 7-week-old (h) and 12.5-week-old (i) mice compared to those from 2.5-week-old mice. P values were determined by a chi-squared test (f,g) and Fisher's exact test corrected with the Benjamini–Hochberg method (h,i).



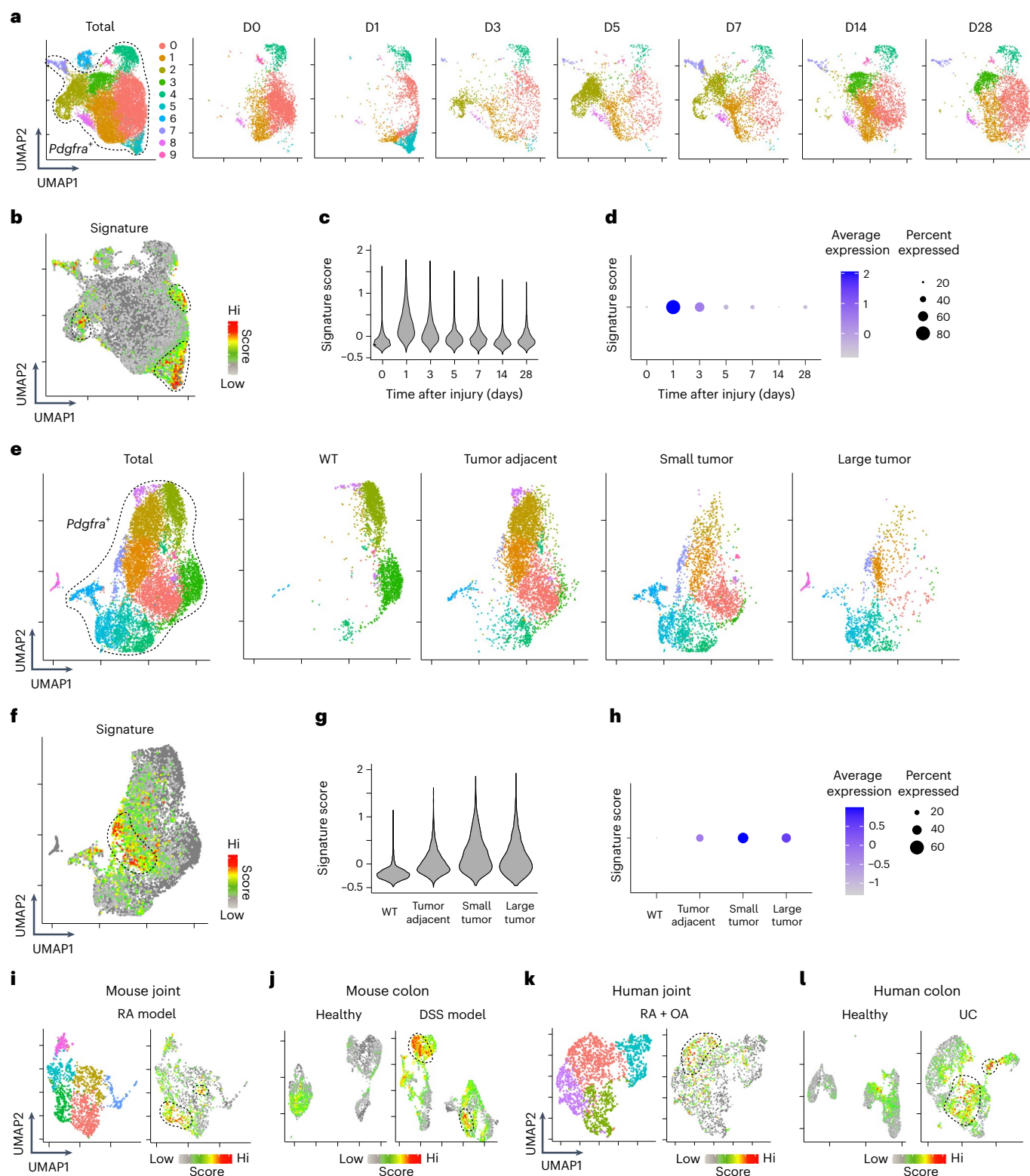


Fig. 8 | The inflammatory MmSC module appears in numerous tissues and pathologies in both mice and human datasets. **a–d**, scRNA-seq of mouse heart tissue at homeostasis (D0) and at D1, D3, D5, D7, D14 and D28 following myocardial infarction⁵⁴. UMAP plots of *Pdgfra*⁺ cells as a whole and by time point (a). Same plot as (a) overlain with the 25-gene CTX-inflammatory signature (b). Violin plot (c) and dot-plot (d) of the inflammatory signature across time points. **e–h**, Mouse scRNA-seq of *Pdgfra*⁺ cells from healthy pancreas tissue and pancreatic ductal adenocarcinoma tumors at various stages of tumor progression⁵⁵. Organized as per **a–d**. **i**, Mouse scRNA-seq of *Pdgfra*⁺ cells from the inflamed joints of the serum transfer induced arthritis model⁵⁶. UMAP plot

of all cells (left) and cells overlain with the 25-gene CTX-inflammatory signature (right). **j**, Mouse scRNA-seq of *Pdgfra*⁺ cells from colons of healthy mice and mice treated with dextran sodium sulfate (DSS)⁵⁷. UMAP plot of cells from healthy (left) and DSS-treated (right) mice overlain with the 25-gene CTX-inflammatory signature. **k**, scRNA-seq of *PDGFRA*⁺ cells from patients with RA or OA⁵⁸. UMAP plot of all cells (left) and cells overlain with the 25-gene CTX-inflammatory signature (right). **l**, scRNA-seq of *PDGFRA*⁺ cells from colonic samples of healthy individuals and patients with UC⁵⁷. UMAP plot of cells from healthy colon (left) and UC-colon (right) overlain with the 25-gene CTX-inflammatory signature.

Finally, we analyzed two recently published human scRNA-seq datasets. The first was of B cells (CD45⁺CD3⁺CD19⁺), T cells (CD45⁺CD3⁺), monocytes (CD45⁺CD14⁺) and stromal fibroblasts (CD45⁺CD31⁺PDPN⁺) isolated from patients with either RA or osteoarthritis (OA)⁵⁸. In the metadata associated with this dataset, all cells were classified as one of these four types and were then sub-classified into subtypes that were examined in greater detail. Stromal fibroblasts were divided into four subtypes. We extracted all stromal fibroblasts, clustered the cells and visualized the data with a UMAP plot (Fig. 8k). All of these clusters were PDGFRA⁺. One cluster, SC-F2, was enriched for the 25-gene CTX-inflammatory signature. This subtype was noted in the original paper to be overabundant in leukocyte-rich RA, compared to leukocyte-poor RA and OA. The second human dataset contained CD45⁺EPCAM⁺CD235a⁺ cells sorted from colonic tissues originating from either healthy individuals or patients with ulcerative colitis (UC)⁵⁷. For each condition, PDGFRA⁺ clusters were extracted, cells were re-clustered and UMAP plots were overlain with the 25-gene CTX-inflammatory signature (Fig. 8l). Cells from healthy human tissues had low signature scores, whereas those from patients with UC showed specific areas enriched for the signature.

Discussion

Time-resolved scRNA-seq provided a dynamic view of how stromal cells communicate with immunocytes in response to acute skeletal muscle injury. Our results highlight an inflammatory MmSC subtype, expressing an impressive array of incendiary mediators that appeared acutely after CTX-induced injury and waned as the response to injury progressed. *Cxcl5*, the transcript most highly induced in MmSCs on D1 after injury and a transcript specifically expressed by this subtype, encoded a mediator with a non-redundant impact on the recruitment of NFs to injured muscle. In the absence of CXCL5 during the initial phase of the injury response, there was persistent inflammation at the later stages and tissue regeneration was hindered. Stromal-cell subtypes expressing the highlighted inflammatory program were detected in a diverse set of tissues and pathologies in both mice and humans, supporting the generality of our observations.

Unlike most immunocyte types that infiltrate muscle tissue from the circulation in response to a perturbation, MmSCs are primarily resident cells, scattered throughout the tissue²⁴. This feature, coupled with their rapid, direct response to parenchymal damage and sensitivity to key inflammatory signals render them ideal ‘early responders’ to tissue insults. MmSCs had additive, discordant or redundant responses to these signals, demonstrating a capacity to direct different flavors of inflammatory responses upon perturbations associated with distinct milieus. Additionally, their ability to transcribe a battery of chemokines, cytokines and other mediators capable of inciting a diversity of target cells could be important in orchestrating a coordinated, multi-immunocyte injury response. Notably, while most MmSCs showed similar high chromatin-accessibility levels at signature inflammatory gene loci at homeostasis, a small, discrete subset emerged as a highly inflammatory subtype within a day of injury. Imaging supported a scenario wherein the stromal support system across the tissue was prepared to respond to injury, but it was the cells closest to the lesion that took on the distinct inflammatory phenotype. Such a scenario would also explain why inflammatory MmSCs disappeared as the lesion resolved and why the injury response remained asymmetrical.

Although some MmSC mediators are stroma-specific, many (though not CXCL5) are also produced by immunocytes (Extended Data Fig. 5), suggesting that MmSCs might also be signal amplifiers. The timeframe in which the various cell sources produce these mediators could be critical; alternatively, the collective level of a mediator might be essential for optimal tissue repair/regeneration. Regardless of why there is this redundancy, it is unlikely to be by accident given the critical role of these mediators during injury. For example, genetic

ablation of the *Ccl2* gene or the gene encoding its receptor, *Ccr2*, results in decreased MF recruitment following muscle injury and impaired tissue regeneration^{59–62}; however, CCR2 also occurs on MuSCs and its activity has been linked to inhibition of MuSC fusion during injury, illustrating how these inflammatory mediators may also have functions that extend outside of their non-canonical roles⁶³.

A comparable MmSC subtype emerged in the mouse model of muscle dystrophy, wherein there is chronic muscle injury. In contrast to the acute setting, where it was beneficial, the inflammatory MmSC subtype was likely deleterious in this disease associated with pathogenic inflammation. Given that disease pathogenesis entails repetitive contraction-induced muscle injury, MmSCs might still function as ‘early responders’ to tissue injury and signal amplifiers; however, these signals likely contribute to the maladaptive chronic inflammation within the tissue as well.

Our study entailed some difficult challenges. A major issue was the lack of tools to study and manipulate MmSCs in vivo. While mice have recently been engineered to deplete all *Pdgfra*-expressing cells in skeletal muscle^{21,22}, ablating more specific populations, like the inflammatory subtype remains problematic due to the lack of appropriate Cre mouse lines. As an alternative approach, we targeted a gene specifically expressed by this subtype to genetically tag the cells with a unique surface molecule susceptible to antibody-mediated depletion. Specifically, we generated a mouse line coupling *Il6* transcription in *Pdgfra*-expressing cells with Thy1.1 expression for isolation and depletion of inflammatory MmSCs. While an analogous system was used to ablate dendritic cells via anti-Thy1.1 antibody administration⁴⁸, MmSCs proved resistant to depletion, likely due to their expression of Cd55, a complement cascade inhibitor. Instead, we used our line as a reporter and performed transfer experiments of isolated Thy1.1⁺ MmSCs to study their function.

Online content

Any methods, additional references, Nature Portfolio reporting summaries, source data, extended data, supplementary information, acknowledgements, peer review information; details of author contributions and competing interests; and statements of data and code availability are available at <https://doi.org/10.1038/s41590-023-01669-w>.

References

- Robertson, T. A., Grounds, M. D., Mitchell, C. A. & Papadimitriou, J. M. Fusion between myogenic cells in vivo: an ultrastructural study in regenerating murine skeletal muscle. *J. Struct. Biol.* **105**, 170–182 (1990).
- Kuang, S., Kuroda, K., Le, G. F. & Rudnicki, M. A. Asymmetric self-renewal and commitment of satellite stem cells in muscle. *Cell* **129**, 999–1010 (2007).
- Sacco, A. et al. Self-renewal and expansion of single transplanted muscle stem cells. *Nature* **456**, 502–506 (2008).
- von Maltzahn, J., Jones, A. E., Parks, R. J. & Rudnicki, M. A. Pax7 is critical for the normal function of satellite cells in adult skeletal muscle. *Proc. Natl Acad. Sci. USA* **110**, 16474–16479 (2013).
- Sambasivan, R. et al. Pax7-expressing satellite cells are indispensable for adult skeletal muscle regeneration. *Development* **138**, 3647–3656 (2011).
- Lepper, C., Partridge, T. A. & Fan, C. M. An absolute requirement for Pax7-positive satellite cells in acute injury-induced skeletal muscle regeneration. *Development* **138**, 3639–3646 (2011).
- Murphy, M. M. et al. Satellite cells, connective tissue fibroblasts and their interactions are crucial for muscle regeneration. *Development* **138**, 3625–3637 (2011).
- Belcastro, A. N., Arthur, G. D., Albisser, T. A. & Raj, D. A. Heart, liver, and skeletal muscle myeloperoxidase activity during exercise. *J. Appl. Physiol.* **80**, 1331–1335 (1996).

9. Teixeira, C. F. et al. Neutrophils do not contribute to local tissue damage, but play a key role in skeletal muscle regeneration, in mice injected with *Bothrops asper* snake venom. *Muscle Nerve* **28**, 449–459 (2003).
10. Brigitte, M. et al. Muscle resident macrophages control the immune cell reaction in a mouse model of notexin-induced myoinjury. *Arthritis Rheum.* **62**, 268–279 (2010).
11. St Pierre, B. A. & Tidball, J. G. Differential response of macrophage subpopulations to soleus muscle reloading after rat hindlimb suspension. *J. Appl. Physiol.* **77**, 290–297 (1994).
12. Saclier, M. et al. Differentially activated macrophages orchestrate myogenic precursor cell fate during human skeletal muscle regeneration. *Stem Cells* **31**, 384–396 (2013).
13. Tonkin, J. et al. Monocyte/macrophage-derived IGF-1 orchestrates murine skeletal muscle regeneration and modulates autocrine polarization. *Mol. Ther.* **23**, 1189–1200 (2015).
14. Deng, B. et al. IL-10 triggers changes in macrophage phenotype that promote muscle growth and regeneration. *J. Immunol.* **189**, 3669–3680 (2012).
15. De Micheli, A. J. et al. Single-cell analysis of the muscle stem cell hierarchy identifies heterotypic communication signals involved in skeletal muscle regeneration. *Cell Rep.* **30**, 3583–3595 (2020).
16. Oprescu, S. N. et al. Temporal dynamics and heterogeneity of cell populations during skeletal muscle regeneration. *iScience* **23**, 100993 (2020).
17. Arnold, L. et al. Inflammatory monocytes recruited after skeletal muscle injury switch into antiinflammatory macrophages to support myogenesis. *J. Exp. Med.* **204**, 1057–1069 (2007).
18. Burzyn, D. et al. A special population of regulatory T cells potentiates muscle repair. *Cell* **155**, 1282–1295 (2013).
19. Castiglioni, A. et al. FOXP3⁺ T cells recruited to sites of sterile skeletal muscle injury regulate the fate of satellite cells and guide effective tissue regeneration. *PLoS ONE* **10**, e0128094 (2015).
20. Panduro, M., Benoist, C. & Mathis, D. T_{reg} cells limit IFN- γ production to control macrophage accrual and phenotype during skeletal muscle regeneration. *Proc. Natl Acad. Sci. USA* **115**, E2585–E2593 (2018).
21. Wosczyzna, M. N. et al. Mesenchymal stromal cells are required for regeneration and homeostatic maintenance of skeletal muscle. *Cell Rep.* **27**, 2029–2035 (2019).
22. Uezumi, A. et al. Mesenchymal Bmp3b expression maintains skeletal muscle integrity and decreases in age-related sarcopenia. *J. Clin. Invest.* **131**, e139617 (2021).
23. Joe, A. W. et al. Muscle injury activates resident fibro/adipogenic progenitors that facilitate myogenesis. *Nat. Cell Biol.* **12**, 153–163 (2010).
24. Uezumi, A. et al. Mesenchymal progenitors distinct from satellite cells contribute to ectopic fat cell formation in skeletal muscle. *Nat. Cell Biol.* **12**, 143–152 (2010).
25. Uezumi, A. et al. Fibrosis and adipogenesis originate from a common mesenchymal progenitor in skeletal muscle. *J. Cell Sci.* **124**, 3654–3664 (2011).
26. Oishi, T. et al. Osteogenic differentiation capacity of human skeletal muscle-derived progenitor cells. *PLoS ONE* **8**, e56641 (2013).
27. Wosczyzna, M. N., Biswas, A. A., Cogswell, C. A. & Goldhamer, D. J. Multipotent progenitors resident in the skeletal muscle interstitium exhibit robust BMP-dependent osteogenic activity and mediate heterotopic ossification. *J. Bone Miner. Res.* **27**, 1004–1017 (2012).
28. Lemos, D. R. et al. Nilotinib reduces muscle fibrosis in chronic muscle injury by promoting TNF-mediated apoptosis of fibro/adipogenic progenitors. *Nat. Med.* **21**, 786–794 (2015).
29. Kopinke, D., Roberson, E. C. & Reiter, J. F. Ciliary hedgehog signaling restricts injury-induced adipogenesis. *Cell* **170**, 340–351 (2017).
30. Mozzetta, C. et al. Fibroadipogenic progenitors mediate the ability of HDAC inhibitors to promote regeneration in dystrophic muscles of young, but not old Mdx mice. *EMBO Mol. Med.* **5**, 626–639 (2013).
31. Hogarth, M. W. et al. Fibroadipogenic progenitors are responsible for muscle loss in limb girdle muscular dystrophy 2B. *Nat. Commun.* **10**, 2430 (2019).
32. Contreras, O. et al. Connective tissue cells expressing fibro/adipogenic progenitor markers increase under chronic damage: relevance in fibroblast-myofibroblast differentiation and skeletal muscle fibrosis. *Cell Tissue Res.* **364**, 647–660 (2016).
33. Ieronimakis, N. et al. PDGFR α signalling promotes fibrogenic responses in collagen-producing cells in Duchenne muscular dystrophy. *J. Pathol.* **240**, 410–424 (2016).
34. Mazala, D. A. et al. TGF- β -driven muscle degeneration and failed regeneration underlie disease onset in a DMD mouse model. *JCI Insight* **5**, e135703 (2020).
35. Lukjanenko, L. et al. Aging disrupts muscle stem cell function by impairing matricellular WISP1 secretion from fibro-adipogenic progenitors. *Cell Stem Cell* **24**, 433–446 (2019).
36. Iezzi, S. et al. Deacetylase inhibitors increase muscle cell size by promoting myoblast recruitment and fusion through induction of follistatin. *Dev. Cell* **6**, 673–684 (2004).
37. Reggio, A. et al. Adipogenesis of skeletal muscle fibro/adipogenic progenitors is affected by the WNT5a/GSK3/ β -catenin axis. *Cell Death Differ.* **27**, 2921–2941 (2020).
38. Fiore, D. et al. Pharmacological blockage of fibro/adipogenic progenitor expansion and suppression of regenerative fibrogenesis is associated with impaired skeletal muscle regeneration. *Stem Cell Res.* **17**, 161–169 (2016).
39. Calve, S., Odelberg, S. J. & Simon, H. G. A transitional extracellular matrix instructs cell behavior during muscle regeneration. *Dev. Biol.* **344**, 259–271 (2010).
40. Pisconti, A. et al. Syndecan-3 and notch cooperate in regulating adult myogenesis. *J. Cell Biol.* **190**, 427–441 (2010).
41. Silver, J. S. et al. Injury-mediated stiffening persistently activates muscle stem cells through YAP and TAZ mechanotransduction. *Sci. Adv.* **7**, eabe4501 (2021).
42. Gilbert, P. M. et al. Substrate elasticity regulates skeletal muscle stem cell self-renewal in culture. *Science* **329**, 1078–1081 (2010).
43. Buechler, M. B. et al. Cross-tissue organization of the fibroblast lineage. *Nature* **593**, 575–579 (2021).
44. Scott, R. W. et al. Hic1 defines quiescent mesenchymal progenitor subpopulations with distinct functions and fates in skeletal muscle regeneration. *Cell Stem Cell* **25**, 797–813 (2019).
45. Tidball, J. G. Regulation of muscle growth and regeneration by the immune system. *Nat. Rev. Immunol.* **17**, 165–178 (2017).
46. Buechler, M. B., Fu, W. & Turley, S. J. Fibroblast-macrophage reciprocal interactions in health, fibrosis, and cancer. *Immunity* **54**, 903–915 (2021).
47. Schreiber, H. A. et al. Intestinal monocytes and macrophages are required for T cell polarization in response to Citrobacter rodentium. *J. Exp. Med.* **210**, 2025–2039 (2013).
48. Heink, S. et al. Trans-presentation of IL-6 by dendritic cells is required for the priming of pathogenic TH17 cells. *Nat. Immunol.* **18**, 74–85 (2017).
49. Mei, J. et al. CXCL5 regulates chemokine scavenging and pulmonary host defense to bacterial infection. *Immunity* **33**, 106–117 (2010).
50. Mann, A. O. et al. IL-17A-producing $\gamma\delta$ T cells promote muscle regeneration in a microbiota-dependent manner. *J. Exp. Med.* **219**, e20211504 (2022).

51. Seo, B. R. et al. Skeletal muscle regeneration with robotic actuation-mediated clearance of neutrophils. *Sci. Transl. Med.* **13**, eabe8868 (2021).
52. Horckmans, M. et al. Neutrophils orchestrate post-myocardial infarction healing by polarizing macrophages towards a reparative phenotype. *Eur. Heart J.* **38**, 187–197 (2017).
53. Aguilar, C. A. et al. In vivo monitoring of transcriptional dynamics after lower-limb muscle injury enables quantitative classification of healing. *Sci. Rep.* **5**, 13885 (2015).
54. Forte, E. et al. Dynamic interstitial cell response during myocardial infarction predicts resilience to rupture in genetically diverse mice. *Cell Rep.* **30**, 3149–3163 (2020).
55. Dominguez, C. X. et al. Single-cell RNA sequencing reveals stromal evolution into LRRC15⁺ myofibroblasts as a determinant of patient response to cancer immunotherapy. *Cancer Discov.* **10**, 232–253 (2020).
56. Croft, A. P. et al. Distinct fibroblast subsets drive inflammation and damage in arthritis. *Nature* **570**, 246–251 (2019).
57. Kinchen, J. et al. Structural remodeling of the human colonic mesenchyme in inflammatory bowel disease. *Cell* **175**, 372–386 (2018).
58. Zhang, F. et al. Defining inflammatory cell states in rheumatoid arthritis joint synovial tissues by integrating single-cell transcriptomics and mass cytometry. *Nat. Immunol.* **20**, 928–942 (2019).
59. Warren, G. L. et al. Chemokine receptor CCR2 involvement in skeletal muscle regeneration. *FASEB J.* **19**, 413–415 (2005).
60. Contreras-Shannon, V. et al. Fat accumulation with altered inflammation and regeneration in skeletal muscle of CCR2^{-/-} mice following ischemic injury. *Am. J. Physiol. Cell Physiol.* **292**, C953–C967 (2007).
61. Shireman, P. K. et al. MCP-1 deficiency causes altered inflammation with impaired skeletal muscle regeneration. *J. Leukoc. Biol.* **81**, 775–785 (2007).
62. Martinez, C. O. et al. Regulation of skeletal muscle regeneration by CCR2-activating chemokines is directly related to macrophage recruitment. *Am. J. Physiol. Regul. Integr. Comp. Physiol.* **299**, R832–R842 (2010).
63. Blanc, R. S. et al. Inhibition of inflammatory CCR2 signaling promotes aged muscle regeneration and strength recovery after injury. *Nat. Commun.* **11**, 4167 (2020).

Publisher's note Springer Nature remains neutral with regard to jurisdictional claims in published maps and institutional affiliations.

Springer Nature or its licensor (e.g. a society or other partner) holds exclusive rights to this article under a publishing agreement with the author(s) or other rightsholder(s); author self-archiving of the accepted manuscript version of this article is solely governed by the terms of such publishing agreement and applicable law.

© The Author(s), under exclusive licence to Springer Nature America, Inc. 2023

Methods

Mice

B6.*Foxp3-IRES-GFP* (*Foxp3*^{GFP}) mice⁶⁴ were obtained from V. Kuchroo (Brigham and Women's Hospital). C57BL/6J (B6, Jax 000664) mice were purchased from The Jackson Laboratory and bred in-house. The B6.Cg-*Tg(CAG-tdKaede)15Utr* (Kaede) mouse line⁶⁵ was obtained from O. Kanagawa. The IL-6 reporter/deleter (*Il6*RD; *Il6*^{tm3307(Cerulean-P2A-CD90.1)Arte}) mouse line⁴⁸ was provided by T. Korn (Technical University of Munich) and was crossed to the C57BL/6-*Tg(Pdgfra-Cre)1Clc/J* (*Pdgfra-Cre*, Jax 013148) mouse line. C57BL/6-*Tg(Csf1r-HBEGF/mCherry)1Mnz/J* (*Csf1r*^{L^{sl-DTR}}, Jax 024046) and B6.129P2-*Lyz2*^{tm1(cree)lfo/J} (*Lysm*^{Cre}, Jax 004781) were purchased from The Jackson Laboratory and crossed together to generate *Lysm*^{Cre} *X* *Csf1r*^{L^{sl-DTR}} mice. D2.B10 (DBA/2-congenic) *Dmd*^{mdx} (*mdx*, Jax 013141) and DBA/2J (CTL, Jax 000671) mice were purchased from The Jackson Laboratory. C;129S2-*Il1b*^{tm1Dch}/MerJ (*Il1b* knockout, Jax 034447) mice were purchased from The Jackson Laboratory and crossed to the suggested control line BALB/cByJ (BALB/c, Jax 001026). Heterozygotes were crossed to each other to produce littermates either homozygous for the knockout allele or WT allele. Mice were used at the ages specified in the figure legends. Experiments were conducted under protocols approved by Harvard Medical School's Institutional Animal Care and Use Committee and housed in specific-pathogen-free facilities at Harvard Medical School.

Mouse treatments

For CTX-induced muscle injury, mice were anesthetized with i.p. injection of ketamine:xylazine in combination (10 mg kg⁻¹:2 mg kg⁻¹) and subsequently were injected with 0.03 ml *Naja mossambica* CTX (0.03 mg ml⁻¹; Sigma-Aldrich) i.m. in one or more hindlimb muscles (tibialis anterior, gastrocnemius and quadriceps), as previously described¹⁸.

For gain-of-function in vivo cytokine injections, recombinant IL-1 β (Peprotech, AF-211-11B, 0.25 μ g per injection), TNF- α (Peprotech, AF-315-01A, 1 μ g per injection), IL-17A (Peprotech, 210-17, 0.5 μ g per injection) and OSM (BioLegend, 762806, 10 μ g per injection) were administered i.p. either individually, in pairs or all four together. The i.p. injection of PBS was used as a control. Uninjured hindlimb muscles were collected at 2 h post-injection unless otherwise specified.

For neutralization of IL-1 β , TNF- α and OSM, anti-IL-1 β antibody (BioXCell, BE0246), anti-TNF α antibody (BioXCell, BE0058) and anti-OSM antibody (R&D, AF-495-NA) or Armenian hamster IgG (BioXCell, BE0091), rat IgG1 (BioXCell, BE0088) and goat IgG (R&D, AB-108-C) isotype controls were used. Then, 200 μ g, 500 μ g and 50 μ g of anti-IL-1 β , anti-TNF- α and anti-OSM antibody, respectively or the same quantity of matched isotype controls, were administered i.p. 24 h before injury and i.m. coincident with CTX injection.

For NF depletion, anti-Ly-6G monoclonal antibody (BioXCell, BE0075-1) or rat IgG2a isotype control (BioXCell, BE0089) was used. Then, 400 μ g, 100 μ g and 100 μ g of antibody was administered i.p. 2 d before injury, i.p. 1 d before injury and i.m. coincident with CTX injection, respectively. For MF depletion, *Lysm*^{Cre} *X* *Csf1r*^{L^{sl-DTR}} mice or their *Lysm*^{wt} *X* *Csf1r*^{L^{sl-DTR}} littermate controls were i.p. injected with DT (D0564; Sigma-Aldrich) in PBS at 20 and 4 ng g⁻¹ at 36 and 12 h before CTX-induced injury, respectively.

For neutralization of CXCL5, anti-CXCL5 monoclonal antibody (R&D Systems, MAB433) or rat IgG2b isotype control (R&D Systems, MAB0061) was used. For collecting tissue 1 d after CTX-induced injury, 40 μ g of antibody was administered i.p. 12 h before injury and i.m. coincident with CTX injection. For collecting tissue 7 d after CTX-induced injury, 40 μ g of antibody was administered i.p. 12 h before injury, i.m. coincident with CTX injection and i.p. at 1 and 2 d after injury.

Cell isolations

Isolation of cells for experiments presented in Figs. 1, 2, 4b, 5a–c and 7 and Extended Data Figs. 2a, 4a,c and 5 was performed as previously

described⁶⁶. Briefly, hindlimb muscles were excised, minced and digested in collagenase VIII (2 mg ml⁻¹, Invitrogen) and dispase (0.5 mg ml⁻¹, Gibco17105-041) for 30 min at 37 °C, then filtered through a 70- μ m filter and washed twice before resuspension in staining medium. The remaining experiments were performed as previously described⁶⁷. Briefly, hindlimb muscles were excised, minced and digested for 90 min at 37 °C in collagenase II (800 U ml⁻¹, Gibco17101-015) in 10 ml per sample of dissociation buffer (Ham's F10 medium supplemented with 10% horse serum and 1% penicillin/streptomycin). Samples were washed with 50 ml dissociation buffer, triturated and then digested for 30 min at 37 °C in collagenase II (200 U ml⁻¹) and dispase (11 U ml⁻¹) in 10 ml per sample of dissociation buffer. Cell suspensions were passed through a 20-gauge needle ten times, washed, filtered through a 40- μ m cell strainer, then washed and stained for analysis or sorting by flow cytometry.

Flow cytometry

The following antibodies were used for flow cytometric staining: CD45 (30-F11), CD11b (M1/70), CD31 (MEC13.3), Sca-1 (Ly6A/E; D7), PDGFR α (CD140a; APA5), VCAM-1 (CD106; 429), Ly-6G (1A8), Ly-6C (HK1.4), Gr-1 (RB6-8C5), F4/80 (BM8), CD64 (X54-5/7.1), CD11c (N418), CD19 (6D5) and TNF- α (MP6-XT22) from BioLegend; IL-1 β (Pro-form, NJTEN3) and Foxp3 (FJK-16s) from Invitrogen; Thy1.1 (CD90.1; OX-7), Thy1.2 (CD90.2; 53-2.1), MyoG (F5D) and Ki-67 (B56) from BD Pharmingen; and anti-TCR- β (H57-597) from BD Horizon. Surface staining was performed at 4 °C for 25 min (previous extra step for IL-1 β and TNF- α staining, see paragraph below). Cells were washed and either DAPI (4',6-diamidino-2-phenylindole) or LIVE/DEAD Fixable Viability Dye (Thermo Fisher Scientific, as per the manufacturer's protocol) was used to mark live and dead cells for fluorescence-activated cell sorting (FACS) or flow cytometry analysis, respectively. Intracellular staining was performed using the eBiosciences Intracellular Fixation & Permeabilization buffer set per manufacturer's protocol. Flow cytometry was performed on a FACSymphony cytometry (BD Biosciences) and FACS on a FACSAria. Data were analyzed using FlowJo software.

For IL-1 β and TNF- α staining, cells were incubated for 3.5 h at 37 °C in complete RPMI-1640 medium supplemented with 10% fetal bovine serum (Thermo Fisher Scientific) and 1 \times protein transport inhibitor cocktail (eBioscience, 00-4980-03). Cells were washed and then stained as detailed above.

Manipulation of cells ex vivo

For co-culture experiments, 40,000 cytofluorimetrically sorted MmSCs were seeded in the bottom level of 24-well Transwell plates (Corning 3422). To compare MmSC responses to co-culture with healthy versus injured myofibers, single myofibers were isolated from extensor digitorum longus (EDL) muscles by incubation in digestion buffer (Ham's F10, 10% horse serum and collagenase II (800 U ml⁻¹; Gibco) for 75 min at 37 °C. Care was taken to touch only tendons of the EDL to prevent damage to myofibers. After digestion, muscles were transferred to warm wash medium (digestion buffer without collagenase, with 10 mM HEPES) in a serum-coated 10-cm Petri dish. Myofibers were released by flushing EDL muscles with wash medium using a flame-polished, serum-coated glass pipette. Healthy myofibers, or fibers with a straight, non-contracted morphology, were transferred to new serum-coated Petri dishes with fresh, warmed wash medium. One dish of fibers was challenged with 10 μ M CTX for 10 min at 37 °C. CTX-treated fibers were washed once in wash medium and 10–15 fibers were subsequently transferred to the upper level of the Transwell system. An equal number of healthy myofibers were included as controls. MmSCs and myofibers were co-cultured in complete medium (Ham's F10, 10% FBS, 2 mM sodium pyruvate, 2 mM L-glutamine and 10 mM HEPES and penicillin/streptomycin) for 24 h before supernatants were collected for ELISA.

ELISA

Cell culture supernatants were spun down (5 min at 400g), diluted appropriately in 5% BSA and assayed for IL-6 using a standard ELISA kit (BioLegend 431304) according to the manufacturer's instructions. Supernatants were analyzed from two independent experiments with conditions performed in duplicate or triplicate. Relative IL-6 concentrations were calculated as the FC in IL-6 in stimulated or co-cultured cells compared to unstimulated cells within an experiment.

Immunofluorescence of muscle sections

Tibialis anterior muscles were excised from *Il6RD × Pdgfra-Cre* mice 2 d following CTX-induced injury. Tissues were placed in chilled 4% paraformaldehyde (Sigma) and stored at 4 °C overnight. Excess paraformaldehyde was then removed, and the tissues were placed in OCT compound (Sakura) within small cryomolds (Fisher Scientific). The 2-methylbutane was cooled using liquid nitrogen and samples were then submerged in the 2-methylbutane until completely frozen. Samples were stored at -80 °C until sectioned. For staining, muscle sections were rinsed and permeabilized in PBS plus 0.05% Tween-20 (PBS-T), blocked for 30 min in PBS-T plus 5% donkey serum and incubated with goat anti-mouse PDGFR α (R&D, AF1062) overnight at 4 °C. Sections were washed in PBS-T and incubated for 1 h at room temperature in the presence of APC-conjugated anti-Thy1.1 (BioLegend), BV421-conjugated anti-Ly-6G (BioLegend) and Alexa Fluor 594-conjugated donkey anti-goat secondary antibody (Jackson ImmunoResearch). Sections were washed and mounted in ProLong Diamond mountant (Invitrogen) and imaged by spinning-disk confocal microscopy using a Nikon Ti inverted microscope, W1 Yokogawa spinning disk with 50- μ m pinholes and Plan Apo \times 20 air and \times 60 oil objectives. Images were analyzed in ImageJ. All images shown are representative of two independent experiments.

Transfer of MmSCs

Cell suspensions were prepared and stained with antibodies against CD45, CD31, Sca-1, PDGFR α , and Thy1.1 utilizing DAPI to identify viable cells. Using *Il6RD* mice, hindlimb muscles at day 2 or day 4 following CTX-induced injury were excised and processed. Either DAPI⁺CD45⁻CD31⁻Sca-1⁺PDGFR α ⁺Thy1.1⁺ (at day 2) or DAPI⁺CD45⁻CD31⁻Sca-1⁺PDGFR α ⁺Thy1.1⁻ (at day 4) cells were sorted into buffer using FACSaria. Cells were spun down and re-suspended in PBS. Kaede mice were anesthetized with i.p. injection of ketamine:xyazine in combination (10 mg kg⁻¹:2 mg kg⁻¹) and then 200,000 cells were injected i.m. into the quadriceps on both sides. At 16 h later, the quadriceps from the recipient Kaede mice were collected and processed as detailed above except 5 ml was used as the total volume during enzymatic digestions given the lower amount of tissue present.

scRNA-seq

MmSCs were isolated by FACS from hindlimb muscles (tibialis anterior, gastrocnemius and quadriceps) of 6–8-week-old male *Foxp3^{GFP}* mice at homeostasis and at 0.5, 1, 3, 7 and 14 d following CTX-induced injury; 2.5-, 5- and 12.5-week-old male *mdx* mice; or 2.5- and 12.5-week-old male CTL mice. For sequencing of MmSCs from *mdx*/CTL mice, individual samples were tagged (hashed) with DNA-coded anti-biotin antibodies (BioLegend). MmSCs were submitted to the Broad Institute Genomics Platform, which performed encapsulation and library preparation following 10x Genomics protocols.

For the CTX dataset, sequenced reads were aligned, assigned to cells and output as count matrices using Cell Ranger (10x Genomics). scRNA-seq analysis was performed using the Seurat package⁶⁸. Cells from each time point were renamed by appending their time point to each of their cell IDs. Cells were then merged into one large count matrix and initially filtered using gene and unique molecular identifier (UMI) number. Cells retained had >300 genes and >50 UMIs. As in the standard Seurat workflow, gene expression was log-normalized, the top 2,000 variable genes were determined, data were scaled and

centered, and PCA was performed on variable genes. The top 50 PCs were used for FindNeighbors and RunUMAP based on JackStraw and ElbowPlot functions. A resolution of 0.3 was used for FindClusters. MmSCs were sequenced with T_{reg} cells and B cells for additional studies and therefore, *Pdgfra*⁺ clusters were extracted from the rest of the cells. *Pdgfra*⁺ cells were then filtered using stricter criteria. Cells retained had >500 genes, >50 UMIs and <10% of reads that mapped to the mitochondrial genome. Starting with renormalization, the same workflow as described above was used, with 50 PCs and a resolution of 0.3 used for cell clustering. Several small clusters expressing hematopoietic or endothelial/pericyte markers were assumed to be contaminants and removed. Once more, the standard workflow was implemented, but instead, using 60 PCs and a resolution of 0.3 for cell clustering. For day-specific analysis, either D0.5 or D1 cells were extracted from the Seurat object containing filtered *Pdgfra*⁺ cells. The standard workflow was used for re-analysis, with 35 PCs and 0.35 or 0.3 resolution used for clustering D0.5 or D1 cells, respectively.

For the *mdx*/CTL dataset, sequenced reads were demultiplexed, aligned, assigned to cells and output as count matrices using Cell Ranger (10x Genomics). Hash-by-cell matrices were obtained using CITE-seq-count⁶⁹. scRNA-seq analysis was performed using the Seurat package⁶⁸. Hash counts were first normalized. Single cells were assigned to hash groups by high expression of a single hash. Cells lacking hashes or with multiple hashes were removed. Cells were then filtered using gene number, UMI number and percent of reads mapping to the mitochondrial genome. Cells retained had >500 genes, >1,000 UMIs and <10% mitochondrial reads. As in the standard Seurat workflow (also described above), gene expression was log-normalized, the top 2,000 variable genes were determined, data were scaled and centered and PCA was performed on variable genes. The top 60 PCs and 0.6 resolution were used for cell clustering. Several small clusters did not express *Pdgfra* and were assumed to be contaminants and removed. Once more, the standard workflow was implemented, with 60 PCs and a resolution of 0.6 used for cell clustering. For age-specific analysis, cells from either the early or late time point were extracted from the Seurat object containing filtered *Pdgfra*⁺ cells. The standard workflow was used for re-analysis, with 36 PCs and 0.3 resolution and 50 PCs and 0.3 resolution used for clustering cells from early and late time points, respectively. Similarly, the standard workflow was used for re-analyzing cells from only the *mdx* condition, with 50 PCs and 0.3 resolution used for cell clustering.

Signature scores were calculated using the Seurat function AddModuleScore. Cluster-based differential expression was performed using the Seurat function FindMarkers. UMAP density plots were made using the BuenColors package and the kde2d density function in the MASS package. Briefly, density values were computed for each condition and color scales were set according to the same min (0) and max (0.05) density values.

Re-analysis of published scRNA-seq datasets

We re-analyzed five published scRNA-seq datasets^{54–58}. To generate the initial Seurat object for each of these datasets, we followed the authors' analyses as much as possible per details provided in the respective Methods sections. *Pdgfra*⁺ (mouse) or *PDGFRA*⁺ (human) cells were extracted from each dataset and re-clustered to produce final plots.

scATAC-seq

scATAC-seq of MmSCs was re-analyzed from published work⁴⁴. Reads were aligned to the mm10 genome and assigned to cells using Cell Ranger ATAC (v.1.1, 10x Genomics). Aligned reads were converted into a snap file, a hdf5 format for scATAC-seq data, using Snaptools (v.1.4.1 (ref. 70)). Downstream analyses were performed in SnapATAC (v.1.0.0 (ref. 70)) following a published approach⁷¹. Cells with 10^{3.5} to 10⁵ unique reads and 20–75% reads in promoters were kept for analysis. Reads were assigned to 5 kb genomic bins, ENCODE blacklist bins

were removed, and the top 5% of bins (corresponding to housekeeping genes) were removed. Cells with coverage of <1,000 bins after filtering were also removed. Dimensionality reduction was performed in several steps, first reducing the cell-by-bin matrix into a cell-by-cell Jaccard similarity matrix, normalizing for sequencing depth, reducing the similarity matrix using diffusion maps and finally reducing the low-dimensional diffusion matrix into a two-dimensional UMAP for visualization. Several small contaminating clusters with high accessibility at hematopoietic genes were removed. Ultimately, six eigenvectors were retained for UMAP generation and semi-supervised Louvain clustering using accessibility at known MmSC marker genes as a guide. The normalized inflammatory module score was calculated by computing gene scores for each inflammatory gene as $\log_{10}(\text{reads per million} + 1)$ within the gene body, pairing each inflammatory gene to a random, accessibility-matched gene, computing the mean accessibility for inflammatory and control signatures for each cell and normalizing the inflammatory score for each cell as the difference of the mean inflammatory and control scores, with the minimum value set at zero.

Histology

CTX-injured tibialis anterior muscles were dissected and immediately fixed in 10% formalin. Tissues were sectioned by the Rodent Histopathology Core at Harvard Medical School and stained with H&E. Four sections, cut 200- μm apart, were used to represent areas throughout the tissue. Images were acquired with a Nikon Ti inverted microscope. For each mouse, the section with the largest number of regenerating muscle fibers (centrally nucleated fibers) was identified for quantification. For 3–5 representative regions in each section, the cross-sectional areas of individual muscle fibers were calculated by manually tracing fiber circumference using Fiji⁷². Overall, 1,000 fibers were traced per section. Experimenters were blinded to the sample group during the entire process.

RNA-seq library construction, sequencing and data processing

For population-level RNA-seq, samples were double-sorted using FACSria and 1,000 cells from each population were collected into 5 μl Buffer TCL (QIAGEN) containing 1% β -mercaptoethanol (Sigma) in DNA LoBind tubes (Eppendorf). Library construction, sequencing and data processing was according to the Immgen protocol (https://www.immgen.org/img/Protocols/ImmGenULI_RNAseq_methods.pdf). Smart-Seq2 was prepared as previously described^{73,74} with minor modifications. Briefly, total RNA was captured and purified on RNA-Clean XP beads (Beckman Coulter). Polyadenylated messenger RNA was selected using an anchored oligo(dT) primer and converted to complementary DNA via reverse transcription. First-strand cDNA was subjected to limited PCR amplification followed by transposon-based fragmentation using the Nextera XT DNA Library Preparation kit (Illumina). Samples were then PCR-amplified using barcoded primers such that each sample carried a specific combination of Illumina P5 and P7 barcodes and were pooled before sequencing. Paired-end sequencing was performed on an Illumina NextSeq500 (two full NextSeq runs per batch of 96 samples, for 10 M raw reads/sample on average) using $2 \times 38\text{-bp}$ reads with no further trimming.

STAR v.2.7.3a (<https://github.com/alexdobin/STAR/releases>) was used to align reads to the mouse genome (GENCODE GRCm38/mm10 primary assembly and gene annotations v.M25; https://www.gencodegenes.org/mouse/release_M25.html). The ribosomal RNA genes were removed. Gene quantification was calculated by featureCounts (<http://subread.sourceforge.net/>). DESeq2 package (Bioconductor) was used to normalize raw read counts via median of ratios method and then converted to GCT and CLS format. Samples with fewer than 1 million uniquely mapped reads were excluded from normalization.

For whole-muscle RNA-seq, RNA was isolated from tissue during TRIzol (Invitrogen) following the manufacturer's instructions.

Two nanograms of RNA in 5 μl TCL containing 1% β -mercaptoethanol in DNA LoBind tubes was used for library construction, sequencing and data processing, as described above.

Population-level RNA-seq analysis

Transcripts were further filtered by minimal expression and coefficient of variation cutoffs. To visualize transcriptional data, Multiplot Studio (developed by S. Davis, Mathis/Benoist laboratory) or the Heatmaply R package was used.

To calculate whole-muscle gene expression scores for each injury-related pathway, the gene expression matrix was log-transformed and the z score of each gene was calculated. The score_genes function in the scanpy package in Python was then used. Genes assigned to each pathway were obtained from elsewhere⁵³.

Pathway analysis

BioPlanet and KEGG pathway analyses were performed using Enrichr (<https://maayanlab.cloud/Enrichr/>)^{75–77}.

Statistical analysis

For volcano plots, a chi-squared test was used to determine signature significance. For the histogram of fiber areas, Mann–Whitney *U*-tests and K–S tests were used. For pathways analyses, Fisher's exact test and the Benjamini–Hochberg method were used. Otherwise, two-tailed unpaired *t*-tests, one-way or two-way ANOVA with Dunnett's or Tukey's multiple comparisons tests were performed in Prism (v.9.1.0, GraphPad) and displayed as mean \pm s.e.m., unless otherwise noted. **P* < 0.05, ***P* < 0.01, ****P* < 0.001, *****P* < 0.0001. A value of more than three s.d. from the mean was adopted as criteria to exclude outliers and was noted in the relevant figure description. For Figs. 4, 5 and 6, we used fraction of control as the y axis. Jax mice and our in-house B6 mice have different immunocyte set points within the muscle. Repeat experiments showed similar delta values between experimental groups, but the set points for the control groups between experiments were often quite different. Therefore, we divided all points by the average of the control group.

Reporting summary

Further information on research design is available in the Nature Portfolio Reporting Summary linked to this article.

Data availability

New data generated in this paper were deposited in Gene Expression Omnibus database under accession no. [GSE205738](https://www.ncbi.nlm.nih.gov/geo/query/acc.cgi?acc=GSE205738).

Code availability

No custom code was generated for this study. Algorithms used for data processing and analysis are referenced in the Methods.

References

- Bettelli, E. et al. Reciprocal developmental pathways for the generation of pathogenic effector TH17 and regulatory T cells. *Nature* **441**, 235–238 (2006).
- Tomura, M. et al. Monitoring cellular movement in vivo with photoconvertible fluorescence protein 'Kaede' transgenic mice. *Proc. Natl Acad. Sci. USA* **105**, 10871–10876 (2008).
- Wang, K. et al. Neuronal, stromal, and T-regulatory cell crosstalk in murine skeletal muscle. *Proc. Natl Acad. Sci. USA* **117**, 5402–5408 (2020).
- Liu, L., Cheung, T. H., Charville, G. W. & Rando, T. A. Isolation of skeletal muscle stem cells by fluorescence-activated cell sorting. *Nat. Protoc.* **10**, 1612–1624 (2015).
- Hao, Y. et al. Integrated analysis of multimodal single-cell data. *Cell* **184**, 3573–3587 (2021).
- Stoeckius, M. et al. Simultaneous epitope and transcriptome measurement in single cells. *Nat. Methods* **14**, 865–868 (2017).

70. Fang, R. et al. Comprehensive analysis of single cell ATAC-seq data with snapATAC. *Nat. Commun.* **12**, 1337 (2021).
71. Michelson, D. A. et al. Thymic epithelial cells co-opt lineage-defining transcription factors to eliminate autoreactive T cells. *Cell* **185**, 2542–2558 (2022).
72. Schindelin, J. et al. Fiji: an open-source platform for biological-image analysis. *Nat. Methods* **9**, 676–682 (2012).
73. Picelli, S. et al. Smart-seq2 for sensitive full-length transcriptome profiling in single cells. *Nat. Methods* **10**, 1096–1098 (2013).
74. Picelli, S. et al. Full-length RNA-seq from single cells using Smart-seq2. *Nat. Protoc.* **9**, 171–181 (2014).
75. Chen, E. Y. et al. Enrichr: interactive and collaborative HTML5 gene list enrichment analysis tool. *BMC Bioinform.* **14**, 128 (2013).
76. Kuleshov, M. V. et al. Enrichr: a comprehensive gene set enrichment analysis web server 2016 update. *Nucleic Acids Res.* **44**, W90–W97 (2016).
77. Xie, Z. et al. Gene set knowledge discovery with Enrichr. *Curr. Protoc.* **1**, e90 (2021).

Acknowledgements

We thank T. Korn and S. Heink for the IL-6 reporter/deleter line; A. Muñoz-Rojas, G. Wang, T. Xiao, S. Galván-Peña, K. Hattori, A. Ortiz-Lopez, V. Piekarsa, N. Asinovski, F. Chen and S. Nepal for experimental assistance; K. Seddu, A. Baysoy, J. Lee, I. Magill and staff at the Broad Genomics Platform for RNA-seq; A. Muñoz-Rojas, L. Yang, B. Vijaykumar and N. Patel for computational help; C. Laplace for graphics; the Harvard Medical School (HMS) Immunology Flow Core; the HMS MiCRoN Core; the HMS Rodent Histopathology Core; and R.G. Spallanzani, A. Muñoz-Rojas, A. Mann, D. Owen, J. Leon and G. Wang for insightful discussions. This work was funded by National Institutes of Health (NIH) grant R01 AR070334 (D.M.), the JPB Foundation (D.M.) and NIH training

grant T32GM007753 (O.K.Y., D.A.M. and T.J.). B.S.H. was partially supported by a Deutsche Forschungsgemeinschaft fellowship (HA 8510/1) and P.K.L. by F32 AG072874.

Author contributions

O.K.Y., B.S.H. and D.M. conceptualized the study. O.K.Y., B.S.H., P.K.L., D.A.M. and M.M.R. designed and performed experiments. O.K.Y., B.S.H., P.K.L., D.A.M., T.J. and M.M.R. analyzed and interpreted data. O.K.Y., B.S.H. and D.M. wrote the paper, which all authors reviewed. D.M. and C.B. provided supervision. D.M. obtained funding.

Competing interests

The authors declare no competing interests.

Additional information

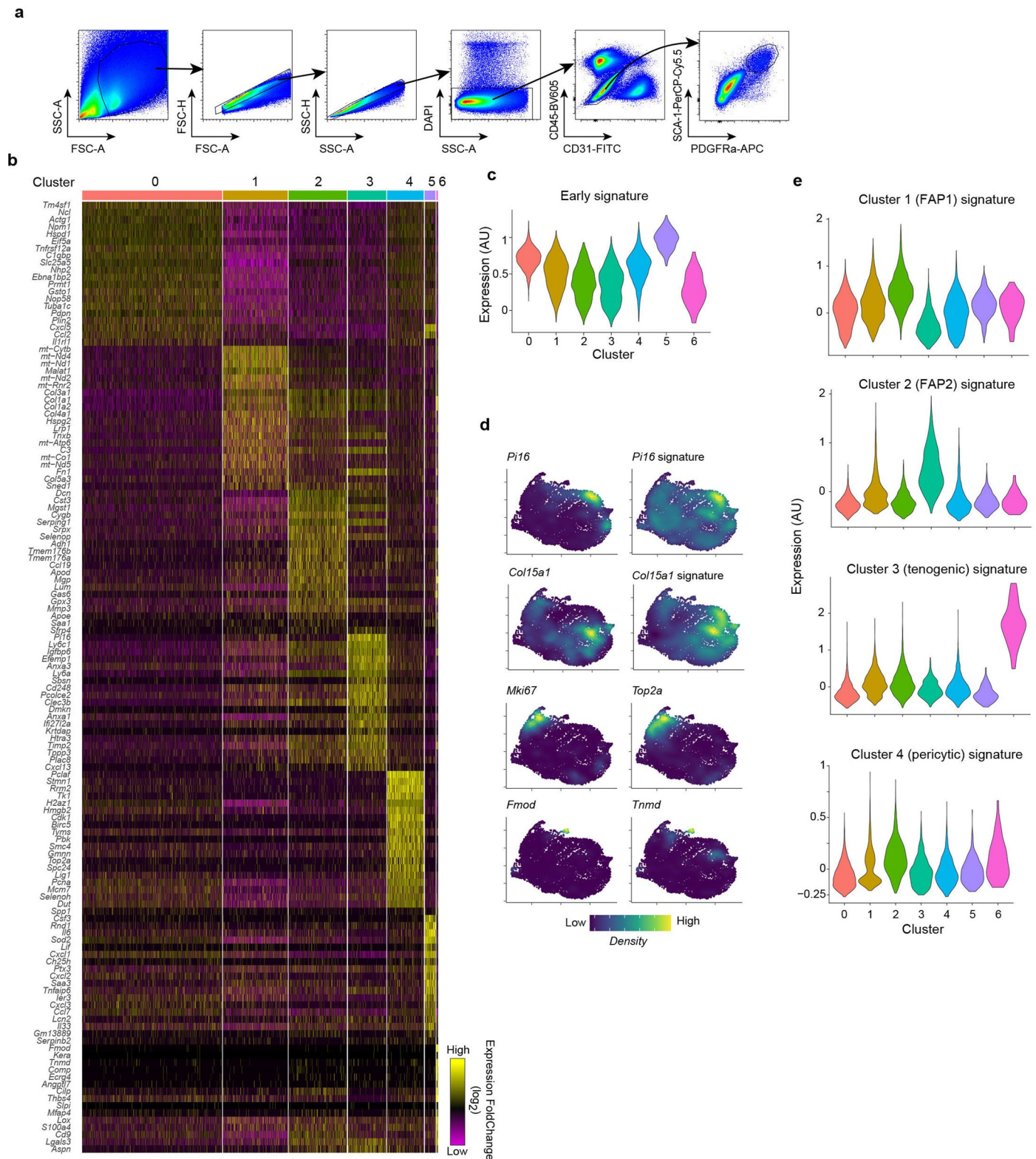
Extended data is available for this paper at <https://doi.org/10.1038/s41590-023-01669-w>.

Supplementary information The online version contains supplementary material available at <https://doi.org/10.1038/s41590-023-01669-w>.

Correspondence and requests for materials should be addressed to Diane Mathis.

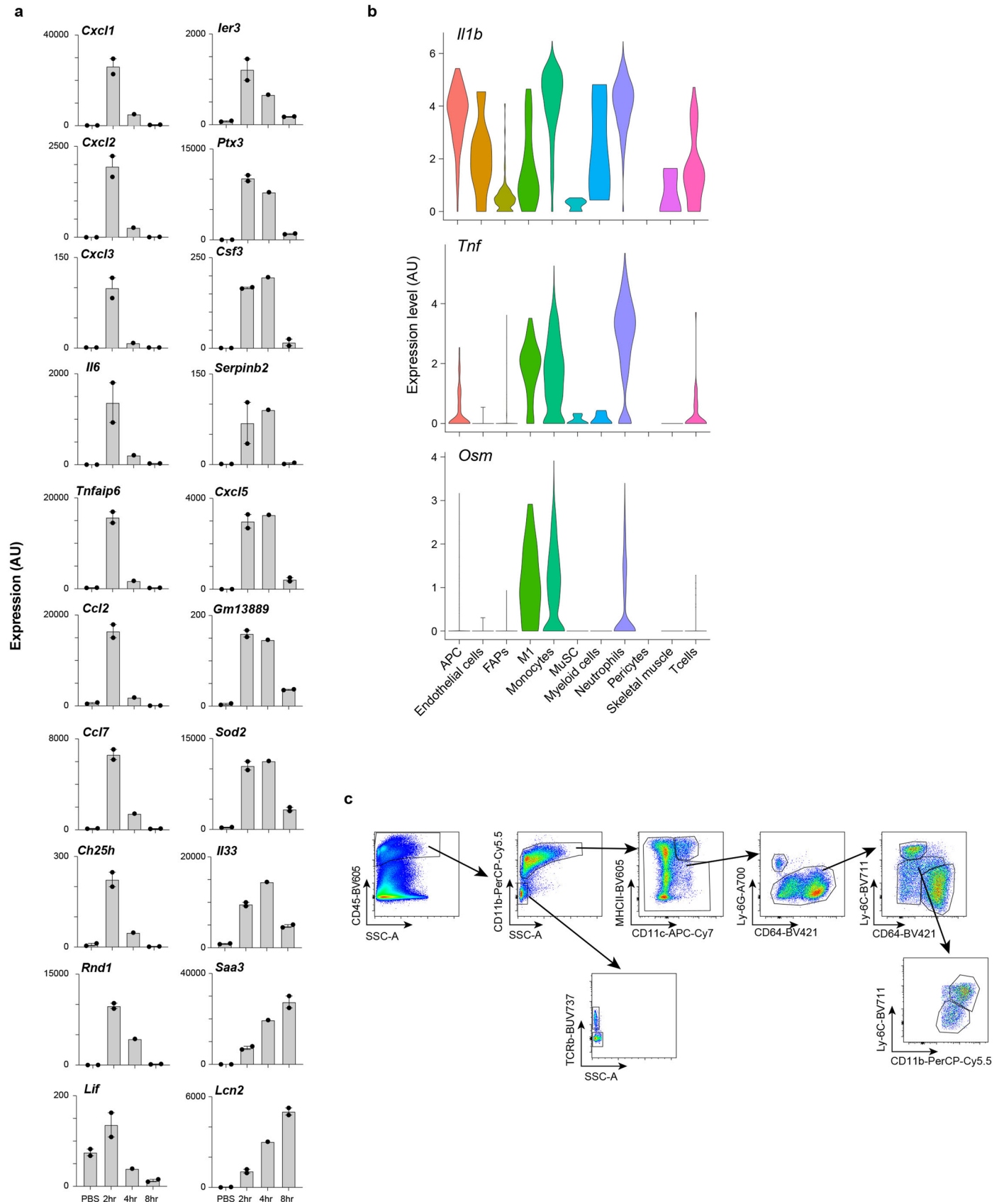
Peer review information *Nature Immunology* thanks the anonymous reviewers for their contribution to the peer review of this work. Primary Handling Editor: S. Houston, in collaboration with the *Nature Immunology* team.

Reprints and permissions information is available at www.nature.com/reprints.



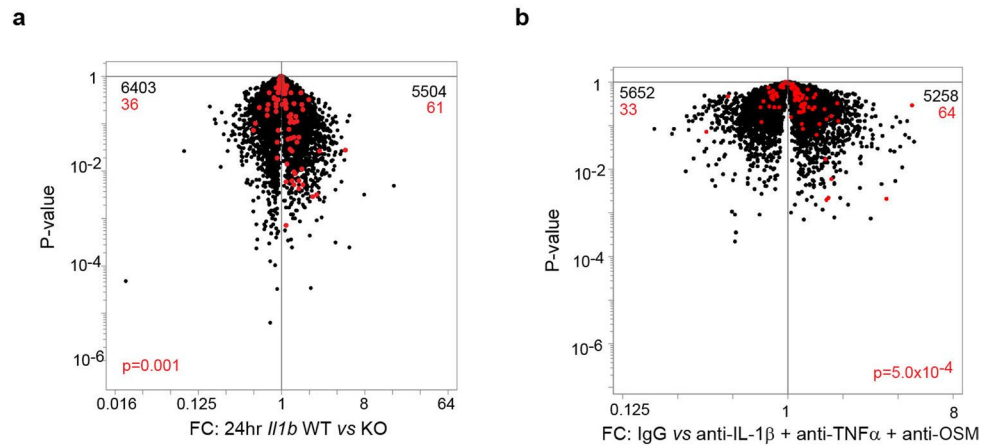
Extended Data Fig. 1 | Identification of an inflammatory MmSC subtype after acute skeletal-muscle injury. **a**, Gating strategy for the cytofluorimetric sorting of MmSCs from hindlimb muscles. **b**, Heat map of the top 200 differentially expressed genes in MmSCs from D1 following CTX-induced injury comparing each cluster *vis-à-vis* all other clusters. **c**, Violin plot of the expression of the early signature (top 100 transcripts distinguishing early time points from the rest)

across all MmSCs clusters on D1 following CTX-induced injury. **d**, Density plot of the expression of the indicated genes and gene signatures in MmSCs from D1 following CTX-induced injury. **e**, Violin plots of the expression of the signatures differentiating the four muscle stromal subtypes from Scott et al.⁴⁴ across all MmSCs clusters on D1 following CTX-induced injury.



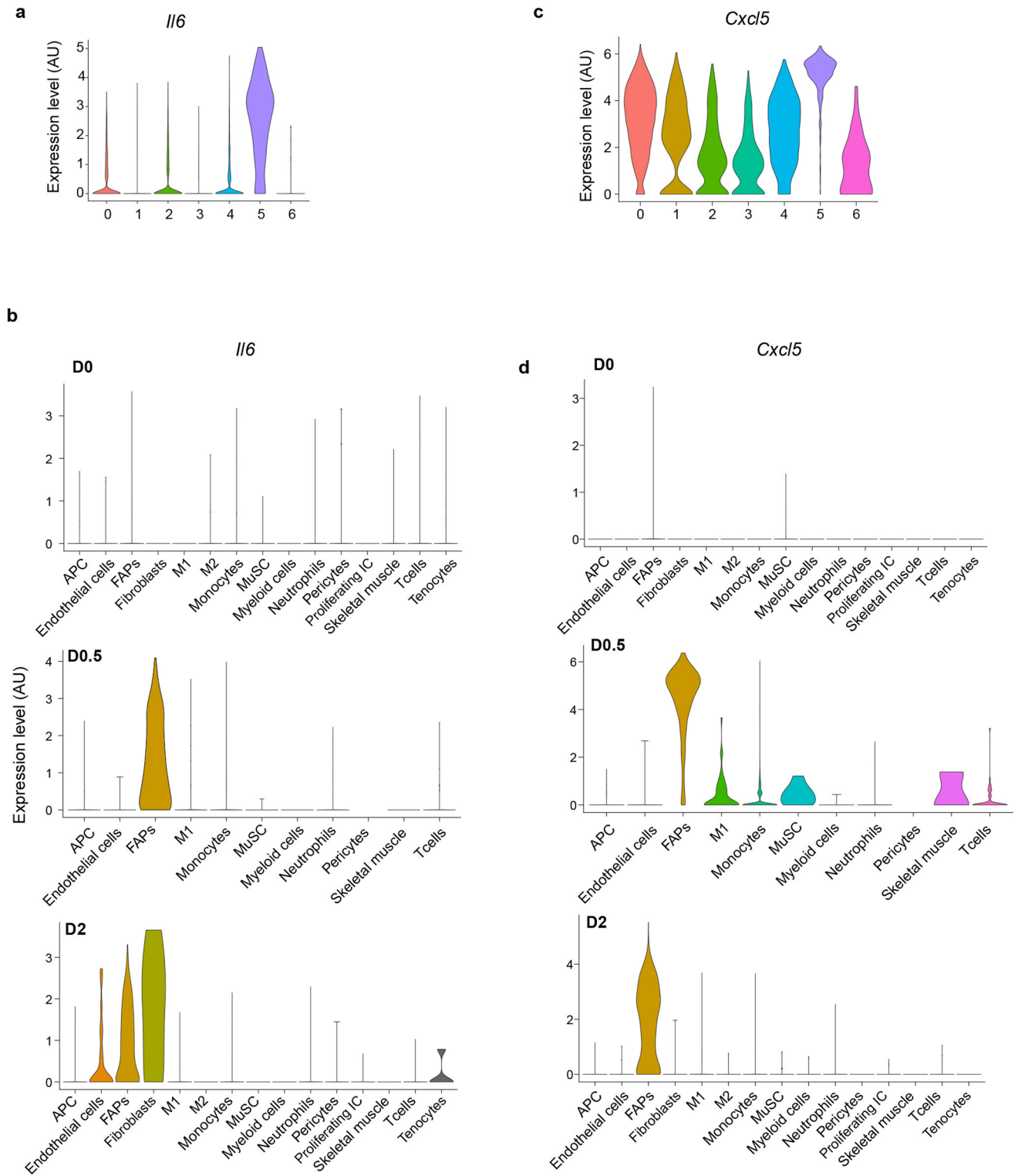
Extended Data Fig. 2 | Role of IL-1 β , TNF α , OSM in inducing MmSC inflammatory program. **a**, Population-level RNA-seq of MmSCs isolated at 2 ($n = 2$), 4 ($n = 1$) or 8 ($n = 2$) hrs after ip co-injection of IL-1 β , TNF α , OSM and IL-17A *vs* after PBS injection ($n = 2$). Expression levels across time points of the top 20 transcripts from the 100-gene inflammatory signature most differentially expressed. Y-axis plot values in arbitrary units. Each data point represents an individual mouse. **b**, Violin plots of *Il1b*, *Tnf* and *Osm* expression across cell

populations in skeletal muscle on D0.5 after CTX-induced injury. scRNA-seq dataset as per¹⁶. Cell nomenclature as per original dataset. **c**, Gating strategy for the cytofluorimetric analysis of diverse immunocyte populations from hindlimb muscles. AU, arbitrary units; APC, antigen-presenting cells; FAPs, fibro/adipogenic progenitors; M1, inflammatory MFs; MuSC, muscle stem cells; PBS, phosphate-buffered saline; FC, fold change.



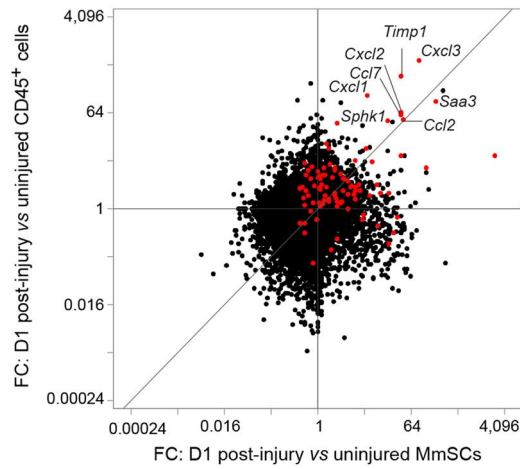
Extended Data Fig. 3 | Impact of the loss of IL-1 β , TNF α and OSM on MmSC inflammatory phenotypes. **a, Population-level RNA-seq of MmSCs isolated from *Il1b* knock-out (KO) ($n = 3$) and wild-type (WT) ($n = 2$) littermates at D1 following CTX-induced injury. Volcano plot comparison of the different conditions. The 100-gene inflammatory signature is shown in red, with numbers**

at the top indicating up- and downregulated transcripts (in comparison with total transcript numbers in black). **b**, Same as (a) except B6 mice were treated with a combination of IL-1 β , TNF α and OSM neutralizing antibodies or IgG isotype controls. P determined by Chi-squared test.



Extended Data Fig. 4 | *Il6* and *Cxcl5* expression in MmSCs at D1 and across skeletal muscle cell populations at homeostasis and various time points after injury. **a**, Violin plot of *Il6* expression across all MmSCs clusters on D1 following CTX-induced injury. **b**, Violin plot of *Il6* expression across cell populations in skeletal muscle at homeostasis, as per¹⁶. **c**, Violin plot of *Cxcl5* expression across

all MmSCs clusters on D1 following CTX-induced injury. **d**, Violin plot of *Cxcl5* expression across cell populations in skeletal muscle at homeostasis, as per¹⁶. M2, reparative MFs; Proliferating IC, proliferating immune cells; other abbreviations as per Extended Data Fig. 2. Cell nomenclature as per original dataset.



Extended Data Fig. 5 | Expression of 100-gene inflammatory signature in immunocytes and MmSCs at homeostasis and upon acute injury. Fold change *vs* fold change plot of population-level RNA-seq of CD45⁺ cells and

MmSCs at D0 and D1 following CTX-induced injury ($n = 3$ per group). The 100-gene inflammatory signature is shown in red. Abbreviations as per Extended Data Fig. 1.

Extended Data Table 1 | CTX-induced inflammatory signatures

	Gene	Fold change (FC)	Cluster 5 - Pct cells gene is detected	Rest of clusters - Pct of cells gene is detected	P-value	Adjusted p-value	avg_log2FC
1	Saa3	19.00	0.80	0.39	6.5E-98	1.7E-93	4.25
2	Csf3	11.69	0.55	0.04	0.0E+00	0.0E+00	3.55
3	Ii6	11.46	0.89	0.27	5.2E-195	1.3E-190	3.52
4	Cxcl2	9.76	0.67	0.20	5.2E-110	1.3E-105	3.29
5	Cxcl1	6.60	0.99	0.78	4.9E-141	1.3E-136	2.72
6	Ptb3	6.55	0.98	0.75	9.3E-122	2.4E-117	2.71
7	Cxcl5	5.54	1.00	0.86	7.5E-145	1.9E-140	2.47
8	Rnd1	5.41	0.78	0.13	6.6E-264	1.7E-259	2.44
9	Cxcl3	5.02	0.51	0.16	3.5E-71	9.1E-67	2.33
10	Tnfrsf6	4.62	0.91	0.57	1.6E-85	4.2E-81	2.21
11	Sox2	4.39	1.00	0.80	2.6E-170	6.7E-166	2.14
12	Serpmb2	3.75	0.17	0.07	1.7E-111	4.5E-07	1.91
13	Ca2	3.11	0.99	0.86	7.1E-65	1.8E-60	1.64
14	Ier3	3.01	0.86	0.44	6.8E-81	1.8E-76	1.59
15	Lcn2	2.97	0.47	0.15	4.2E-56	1.1E-51	1.57
16	Gm13889	2.86	0.27	0.07	4.3E-43	1.1E-38	1.51
17	Ii33	2.85	0.85	0.58	1.9E-53	5.0E-49	1.51
18	Ch25h	2.80	0.42	0.06	7.7E-138	2.0E-133	1.48
19	Cd7	2.57	1.00	0.94	4.4E-59	1.1E-54	1.36
20	Lif	2.53	0.41	0.05	5.7E-169	1.5E-164	1.34
21	Mi2	2.51	1.00	1.00	6.9E-120	1.8E-115	1.33
22	Mt1	2.35	1.00	1.00	1.7E-99	4.4E-95	1.23
23	Timp1	2.34	1.00	0.98	2.1E-72	5.3E-68	1.23
24	Uap1	2.32	0.95	0.78	7.7E-50	2.0E-45	1.22
25	Nkbia	2.27	0.98	0.76	1.2E-74	3.1E-70	1.18
26	Cebpb	2.23	0.99	0.90	5.2E-95	1.3E-90	1.16
27	Ddit4	2.16	0.61	0.20	2.5E-79	6.4E-75	1.11
28	Fst	2.15	0.82	0.48	4.6E-51	1.2E-46	1.10
29	Fth1	2.09	1.00	1.00	7.0E-63	1.8E-58	1.06
30	Adamsl1	2.01	0.79	0.41	1.2E-52	3.0E-48	1.01
31	Hes1	2.00	0.75	0.48	7.9E-24	2.0E-19	1.00
32	Ptgs2	1.97	0.43	0.12	6.0E-63	1.6E-58	0.98
33	Lmcd1	1.92	0.29	0.14	2.5E-14	6.4E-10	0.94
34	Ass1	1.91	0.59	0.32	2.0E-30	5.1E-26	0.93
35	Sox3	1.91	0.89	0.62	1.8E-49	4.7E-45	0.93
36	Tnfrsf1	1.89	0.60	0.18	8.8E-91	2.3E-86	0.92
37	Hif1a	1.86	0.92	0.56	1.6E-55	4.1E-51	0.89
38	Ptges	1.82	0.64	0.30	9.5E-49	2.5E-44	0.86
39	Smim3	1.80	0.75	0.30	3.4E-76	8.7E-72	0.85
40	Zc3h12a	1.79	0.56	0.12	1.4E-122	3.5E-118	0.84
41	Ngf	1.77	0.32	0.14	5.7E-20	1.5E-15	0.82
42	Prg4	1.76	0.96	0.91	8.8E-17	2.3E-12	0.82
43	Cyp7b1	1.74	0.51	0.18	1.8E-51	4.6E-47	0.80
44	Tnc	1.67	0.54	0.34	3.1E-13	8.1E-09	0.74
45	Angptl4	1.66	0.94	0.82	3.6E-28	9.3E-24	0.73
46	Slc39a14	1.66	0.89	0.56	3.8E-49	9.7E-45	0.73
47	Phfda1	1.64	0.90	0.70	1.8E-28	4.6E-24	0.72
48	Cxcl14	1.63	0.98	0.89	8.0E-25	2.1E-20	0.71
49	Inhba	1.63	0.32	0.14	8.0E-21	2.1E-16	0.70
50	Glx	1.62	0.55	0.30	1.2E-27	3.1E-23	0.70

	Gene	Fold change (FC)	Cluster 5 - Pct of cells gene is detected	Rest of clusters - Pct cells gene is detected	P-value	Adjusted p-value	avg_log2FC
51	Id3	1.62	0.92	0.77	9.7E-24	2.5E-19	0.70
52	Serpine1	1.61	0.68	0.48	1.3E-12	3.4E-08	0.69
53	Gch1	1.60	0.48	0.12	1.1E-76	2.8E-72	0.68
54	Hspa5	1.59	0.99	0.95	6.5E-27	1.7E-22	0.66
55	Icam1	1.55	0.59	0.31	9.0E-29	2.3E-24	0.63
56	Adora2b	1.53	0.51	0.24	2.5E-31	6.6E-27	0.61
57	Gpm6b	1.51	0.75	0.43	7.1E-37	1.8E-32	0.60
58	Herpud1	1.51	0.68	0.50	1.0E-15	2.7E-11	0.59
59	Slc16a1	1.50	0.57	0.27	2.8E-35	7.2E-31	0.58
60	Golga3	1.49	0.17	0.11	2.3E-03	1.0E+00	0.58
61	Acs4	1.49	0.59	0.26	2.1E-40	5.3E-36	0.57
62	Tnfrsf1	1.47	0.23	0.04	1.9E-52	4.9E-48	0.56
63	Tm4sf1	1.47	0.88	0.75	3.3E-14	8.6E-10	0.56
64	Pt15	1.46	0.30	0.12	1.9E-21	4.9E-17	0.55
65	Tnfrsf3	1.46	0.25	0.04	6.6E-73	1.7E-68	0.55
66	Eli2	1.46	0.43	0.11	6.5E-70	1.7E-65	0.54
67	Cfb	1.45	0.40	0.16	3.3E-28	8.5E-24	0.54
68	Znrf1	1.45	0.64	0.36	1.3E-28	3.4E-24	0.54
69	Fgf7	1.44	0.46	0.23	6.6E-22	1.7E-17	0.53
70	Cyp1b1	1.44	0.35	0.11	1.1E-39	2.7E-35	0.53
71	Ctsc	1.44	0.52	0.25	6.0E-26	1.6E-21	0.53
72	Rdh10	1.44	0.69	0.48	4.1E-17	1.1E-12	0.52
73	Rnf19b	1.43	0.51	0.20	2.6E-40	6.6E-36	0.52
74	Manf	1.42	0.94	0.90	5.2E-23	1.4E-18	0.51
75	Rgcc	1.42	0.39	0.14	1.1E-35	2.8E-31	0.51
76	Ldha	1.42	0.98	0.92	3.7E-26	9.6E-22	0.51
77	Cebpd	1.42	0.96	0.80	1.3E-20	3.5E-16	0.50
78	Sphk1	1.41	0.64	0.30	5.1E-37	1.3E-32	0.50
79	Ptgn2	1.40	0.56	0.26	4.4E-34	1.1E-29	0.49
80	Dnajb6	1.38	0.77	0.60	2.8E-17	7.1E-13	0.47
81	Slc9a3r1	1.37	0.21	0.04	4.9E-46	1.3E-41	0.46
82	Nkx1	1.37	0.55	0.29	1.2E-22	3.1E-18	0.45
83	Dnajb9	1.36	0.69	0.47	7.9E-19	2.0E-14	0.44
84	Ehd1	1.35	0.68	0.46	1.4E-17	3.5E-13	0.44
85	Trdc	1.35	0.12	0.01	1.2E-68	3.2E-64	0.43
86	Emb	1.35	0.30	0.11	3.4E-23	8.8E-19	0.43
87	Dbx2	1.35	0.20	0.04	1.2E-50	3.2E-46	0.43
88	Zfp361	1.35	0.75	0.54	1.4E-16	3.6E-12	0.43
89	Gm12840	1.35	0.27	0.18	3.6E-05	9.3E-01	0.43
90	Prdx6	1.34	0.89	0.73	5.9E-14	1.5E-09	0.43
91	Clmp	1.34	0.67	0.47	6.4E-17	1.7E-12	0.43
92	Ii1r1	1.33	0.71	0.44	2.0E-20	5.0E-16	0.41
93	Fosl2	1.33	0.54	0.27	4.4E-25	1.1E-20	0.41
94	Mcoln2	1.33	0.35	0.11	1.3E-35	3.4E-31	0.41
95	Mt4	1.33	0.14	0.03	6.4E-24	1.6E-19	0.41
96	Sifn2	1.33	0.33	0.11	1.1E-33	2.9E-29	0.41
97	Sox11	1.32	0.13	0.03	3.2E-21	8.3E-17	0.41
98	Ccn4	1.32	0.40	0.15	2.6E-33	6.8E-29	0.40
99	Alpl	1.31	0.42	0.18	2.7E-26	7.1E-22	0.39
100	Nkxib	1.31	0.58	0.33	7.3E-23	1.9E-18	0.39

25-gene CTX-inflammatory signature
 100-gene CTX-inflammatory signature (includes 25-gene signature)

Reporting Summary

Nature Portfolio wishes to improve the reproducibility of the work that we publish. This form provides structure for consistency and transparency in reporting. For further information on Nature Portfolio policies, see our [Editorial Policies](#) and the [Editorial Policy Checklist](#).

Statistics

For all statistical analyses, confirm that the following items are present in the figure legend, table legend, main text, or Methods section.

- | n/a | Confirmed |
|-------------------------------------|--|
| <input type="checkbox"/> | <input checked="" type="checkbox"/> The exact sample size (n) for each experimental group/condition, given as a discrete number and unit of measurement |
| <input type="checkbox"/> | <input checked="" type="checkbox"/> A statement on whether measurements were taken from distinct samples or whether the same sample was measured repeatedly |
| <input type="checkbox"/> | <input checked="" type="checkbox"/> The statistical test(s) used AND whether they are one- or two-sided
<i>Only common tests should be described solely by name; describe more complex techniques in the Methods section.</i> |
| <input checked="" type="checkbox"/> | <input type="checkbox"/> A description of all covariates tested |
| <input type="checkbox"/> | <input checked="" type="checkbox"/> A description of any assumptions or corrections, such as tests of normality and adjustment for multiple comparisons |
| <input type="checkbox"/> | <input checked="" type="checkbox"/> A full description of the statistical parameters including central tendency (e.g. means) or other basic estimates (e.g. regression coefficient) AND variation (e.g. standard deviation) or associated estimates of uncertainty (e.g. confidence intervals) |
| <input type="checkbox"/> | <input checked="" type="checkbox"/> For null hypothesis testing, the test statistic (e.g. F , t , r) with confidence intervals, effect sizes, degrees of freedom and P value noted
<i>Give P values as exact values whenever suitable.</i> |
| <input checked="" type="checkbox"/> | <input type="checkbox"/> For Bayesian analysis, information on the choice of priors and Markov chain Monte Carlo settings |
| <input checked="" type="checkbox"/> | <input type="checkbox"/> For hierarchical and complex designs, identification of the appropriate level for tests and full reporting of outcomes |
| <input checked="" type="checkbox"/> | <input type="checkbox"/> Estimates of effect sizes (e.g. Cohen's d , Pearson's r), indicating how they were calculated |

Our web collection on [statistics for biologists](#) contains articles on many of the points above.

Software and code

Policy information about [availability of computer code](#)

Data collection

Data analysis

For manuscripts utilizing custom algorithms or software that are central to the research but not yet described in published literature, software must be made available to editors and reviewers. We strongly encourage code deposition in a community repository (e.g. GitHub). See the Nature Portfolio [guidelines for submitting code & software](#) for further information.

Data

Policy information about [availability of data](#)

All manuscripts must include a [data availability statement](#). This statement should provide the following information, where applicable:

- Accession codes, unique identifiers, or web links for publicly available datasets
- A description of any restrictions on data availability
- For clinical datasets or third party data, please ensure that the statement adheres to our [policy](#)

New data generated in this paper were deposited in Gene Expression Omnibus (GEO) database under accession number GSE205738. Mouse reference genome (GRCm38) was used for aligning RNA-seq reads.

Human research participants

Policy information about [studies involving human research participants and Sex and Gender in Research](#).

Reporting on sex and gender	<input type="text" value="N/A"/>
Population characteristics	<input type="text" value="N/A"/>
Recruitment	<input type="text" value="N/A"/>
Ethics oversight	<input type="text" value="N/A"/>

Note that full information on the approval of the study protocol must also be provided in the manuscript.

Field-specific reporting

Please select the one below that is the best fit for your research. If you are not sure, read the appropriate sections before making your selection.

Life sciences Behavioural & social sciences Ecological, evolutionary & environmental sciences

For a reference copy of the document with all sections, see [nature.com/documents/nr-reporting-summary-flat.pdf](https://www.nature.com/documents/nr-reporting-summary-flat.pdf)

Life sciences study design

All studies must disclose on these points even when the disclosure is negative.

Sample size	No statistical methods were used to predetermine sample sizes; however, sample sizes were selected based on previous publications in the field (Hanna et al. Cell 2023; Mann et al. J Exp Med 2022) and are indicated in the figure legends.
Data exclusions	Cells not passing standard quality control thresholds (based on number of unique reads per cell and fraction of reads in peaks) or contaminant cells were excluded from analysis. A value of more than three standard deviations (SDs) from the mean was adopted as criteria to exclude outliers and was noted in the relevant figure description.
Replication	Flow cytometry-based experiments were repeated at least twice. Single cell RNA sequencing analysis was performed once.
Randomization	With wild-type and knock-out mice, randomization was not used as mice were co-housed littermates and genotypes were determined beforehand. In cases where mice were of the same genotype, mice were randomly assigned to experimental groups.
Blinding	Blinding was not performed as animal housing facilities required cage labeling. When possible, investigators would convert sample identities into numbers after harvesting tissue from mice to blind investigators during the course of the experiment and during data collection. For quantification of muscle fiber areas, investigators were blind to the sample groups during image analysis.

Reporting for specific materials, systems and methods

We require information from authors about some types of materials, experimental systems and methods used in many studies. Here, indicate whether each material, system or method listed is relevant to your study. If you are not sure if a list item applies to your research, read the appropriate section before selecting a response.

Materials & experimental systems

n/a	Included in the study
<input type="checkbox"/>	<input checked="" type="checkbox"/> Antibodies
<input checked="" type="checkbox"/>	<input type="checkbox"/> Eukaryotic cell lines
<input checked="" type="checkbox"/>	<input type="checkbox"/> Palaeontology and archaeology
<input type="checkbox"/>	<input checked="" type="checkbox"/> Animals and other organisms
<input checked="" type="checkbox"/>	<input type="checkbox"/> Clinical data
<input checked="" type="checkbox"/>	<input type="checkbox"/> Dual use research of concern

Methods

n/a	Included in the study
<input checked="" type="checkbox"/>	<input type="checkbox"/> ChIP-seq
<input type="checkbox"/>	<input checked="" type="checkbox"/> Flow cytometry
<input checked="" type="checkbox"/>	<input type="checkbox"/> MRI-based neuroimaging

Antibodies

Antibodies used	Biolegend: Anti-CD45-BV605 (Clone: 30-F11; Cat #: 103139; Dilution 1:100)
-----------------	--

Anti-CD11b-PerCP-Cy5.5 (Clone: M1/70; Cat #: 101228; Dilution 1:100)
 Anti-CD11b-PE-Cy7 (Clone: M1/70; Cat #: 101215; Dilution 1:100)
 Anti-CD31-FITC (Clone: MEC13.3; Cat #: 102506; Dilution 1:100)
 Anti-CD31-Pacific Blue (Clone: 390; Cat #: 102421; Dilution 1:100)
 Anti-Ly6A/E-PerCP-Cy5.5 (Clone: D7; Cat #: 108124; Dilution 1:50)
 Anti-CD140a-APC (Clone: APA5; Cat #: 135908; Dilution 1:50)
 Anti-CD106-PE-Cy7 (Clone: 429; Cat #: 105720; Dilution 1:100)
 Anti-Ly-6G-APC-Cy7 (Clone: 1A8; Cat #: 127624; Dilution 1:100)
 Anti-Ly-6G-A700 (Clone: 1A8; Cat #: 127621; Dilution 1:100)
 Anti-Ly-6C-FITC (Clone: HK1.4; Cat #: 128006; Dilution 1:100)
 Anti-Ly-6C-BV711 (Clone: HK1.4; Cat #: 128037; Dilution 1:100)
 Anti-Gr-1-PE (Clone: RB6-8C5; Cat #: 108408; Dilution 1:100)
 Anti-F4/80-A700 (Clone: BM8; Cat #: 123130; Dilution 1:100)
 Anti-CD64-BV421 (Clone: X54-5/7.1; Cat #: 139309; Dilution 1:100)
 Anti-CD11c-PE (Clone: N418; Cat #: 117308; Dilution 1:100)
 Anti-CD11c-APC-Cy7 (Clone: N418; Cat #: 117323; Dilution 1:100)
 Anti-MHCl-BV605 (Clone: M5/114.15.2; Cat #: 107639; Dilution 1:100)
 Anti-CD19-A700 (Clone: 6D5; Cat #: 115528; Dilution 1:100)
 Anti-TNFa-PE (Clone: MP6-XT22; Cat #: 506306; Dilution 1:50)

Invitrogen:

Anti-IL-1b-APC (Clone: NJTEN3; Cat #: 17-7114-80; Dilution 1:33.3)
 Anti-Foxp3-FITC (Clone: FJK-16s; Cat #: 11-5773-82; Dilution 1:50)

BD Pharmingen:

Anti-CD90.1-PE (Clone: OX-7; Cat #: 554898; Dilution 1:100)
 Anti-CD90.2-APC-Cy7 (Clone: 53-2.1; Cat #: 561641; Dilution 1:100)
 Anti-MyoG-PE (Clone: F5D; Cat #: 563120; Dilution 1:100)
 Anti-Ki-67-A700 (Clone: B56; Cat #: 561277; Dilution 1:100)

BD Horizon:

Anti-TCR β -BUV737 (Clone: H57-597; Cat #: 612821; Dilution 1:100)

BioXCell:

Anti-IL-1b (Clone: B122; Cat #: BE0246; 200 ug/mouse)
 Armenian hamster IgG (Polyclonal; Cat #: BE0091; 200 ug/mouse)
 Anti-TNFa (Clone: XT3.11; Cat #: BE0058; 500 ug/mouse)
 Anti-Horseradish peroxidase (Clone: HRPN; Cat #: BE0088; 500 ug/mouse)

R&D Systems:

Anti-Osm (Cat #: AF-495-NA; 50 ug/mouse)
 Goat IgG Control (Cat #: AB-108-C; 50 ug/mouse)

Validation

All antibodies are commercially available and were validated by the respective manufacturer. Validation statements are available online on each manufacturer's website.

Animals and other research organisms

Policy information about [studies involving animals](#); [ARRIVE guidelines](#) recommended for reporting animal research, and [Sex and Gender in Research](#)

Laboratory animals

B6.Foxp3-IRES-GFP (Foxp3GFP) mice were obtained from V. Kuchroo (Brigham and Women's Hospital, Boston, MA). C57BL/6J (B6, Jax #000664) mice were purchased from The Jackson Laboratory and bred in-house. The B6.Cg-Tg(CAG-tdKaede)15Utr (Kaede) mouse line was obtained from O. Kanagawa. The IL-6 reporter/deleter (Il6RD; Il6tm3307(Cerulean-P2A-CD90.1)Arte) mouse line was provided by T. Korn (Technical University of Munich, Munich, Germany) and was crossed to the C57BL/6-Tg(Pdgfra-Cre)1Clc/J (Pdgfra-Cre, Jax #013148) mouse line. C57BL/6-Tg (Csf1r-HBEGF/mCherry)1Mnz/J (Csf1rLsL-DTR, Jax #024046) and B6.129P2-Lyz2tm1(cre)lfo/J (LysmCre, Jax #004781) were purchased from The Jackson Laboratory and crossed together to generate LysmCre X Csf1rLsL-DTR mice. D2.B10 (DBA/2-congenic) Dmdmdx (mdx, Jax #013141) and DBA/2J (CTL, Jax #000671) mice were purchased from The Jackson Laboratory. C;129S2-Il1btm1Dch/MerJ (Il1b KO, Jax #034447) mice were purchased from The Jackson Laboratory and crossed to the suggested control line BALB/cByJ (BALB/c, Jax #001026). Heterozygotes were crossed to each other to produce littermates either homozygous for the knock-out allele or wild-type allele. All mice used were 6- to 9-weeks-old except for mdx and CTL mice, which were used to generate datasets across ages. Ages of mice are listed in the figure legends. All mice were housed in specific-pathogen-free facilities at Harvard Medical School with a 12 hr light/dark cycle, 71 F room temperature, and 50% room humidity.

Wild animals

No wild animals were used in this study.

Reporting on sex

Only male mice were used in this study.

Field-collected samples

No field-collected samples were in this study.

Ethics oversight

Experiments were conducted under protocols approved by Harvard Medical School's Institutional Animal Care and Use Committee.

Note that full information on the approval of the study protocol must also be provided in the manuscript.

Plots

Confirm that:

- The axis labels state the marker and fluorochrome used (e.g. CD4-FITC).
- The axis scales are clearly visible. Include numbers along axes only for bottom left plot of group (a 'group' is an analysis of identical markers).
- All plots are contour plots with outliers or pseudocolor plots.
- A numerical value for number of cells or percentage (with statistics) is provided.

Methodology

Sample preparation

Cells were isolated from mouse skeletal muscle tissues as described in the methods.

Instrument

Flow cytometry was performed on a FACSymphony cytometer (BD Biosciences) and FACS on a FACSAria sorter (BD Biosciences).

Software

Data was acquired with FACSDiva (BD Biosciences) and analyzed using FlowJo software.

Cell population abundance

Sorting purity was >90% based on single cell data analysis or >95-99% based on post-sort flow cytometry verification.

Gating strategy

Gating strategy is provided in Extended Data figures.

- Tick this box to confirm that a figure exemplifying the gating strategy is provided in the Supplementary Information.